Acta Biomaterialia 63 (2017) 350–368

Contents lists available at ScienceDirect

Acta Biomaterialia

journal homepage: www.elsevier.com/locate/actabiomat

Full length article

Mechanical characterization of structurally porous biomaterials built via additive manufacturing: experiments, predictive models, and design maps for load-bearing bone replacement implants

D. Melancon [a], Z.S. Bagheri [a], R.B. Johnston [a], L. Liu [a], M. Tanzer [b], D. Pasini [a,*]

[a] Mechanical Engineering Department, McGill University, Montreal, Quebec H3G 1A4, Canada
[b] Division of Orthopaedics, Department of Surgery, McGill University, Montreal, Quebec H3G 1A4, Canada

ARTICLE INFO

Article history:
Received 4 May 2017
Received in revised form 30 August 2017
Accepted 12 September 2017
Available online 18 September 2017

Keywords:
Structurally porous biomaterial
Mechanical characterization
Additive manufacturing
Design maps
Bone replacement implants

ABSTRACT

Porous biomaterials can be additively manufactured with micro-architecture tailored to satisfy the stringent mechano-biological requirements imposed by bone replacement implants. In a previous investigation, we introduced structurally porous biomaterials, featuring strength five times stronger than commercially available porous materials, and confirmed their bone ingrowth capability in an *in vivo* canine model. While encouraging, the manufactured biomaterials showed geometric mismatches between their internal porous architecture and that of its as-designed counterpart, as well as discrepancies between predicted and tested mechanical properties, issues not fully elucidated. In this work, we propose a systematic approach integrating computed tomography, mechanical testing, and statistical analysis of geometric imperfections to generate statistical based numerical models of high-strength additively manufactured porous biomaterials. The method is used to develop morphology and mechanical maps that illustrate the role played by pore size, porosity, strut thickness, and topology on the relations governing their elastic modulus and compressive yield strength. Overall, there are mismatches between the mechanical properties of ideal-geometry models and as-manufactured porous biomaterials with average errors of 49% and 41% respectively for compressive elastic modulus and yield strength. The proposed methodology gives more accurate predictions for the compressive stiffness and the compressive strength properties with a reduction of the average error to 11% and 7.6%. The implications of the results and the methodology here introduced are discussed in the relevant biomechanical and clinical context, with insight that highlights promises and limitations of additively manufactured porous biomaterials for load-bearing bone replacement implants.

Statement of Significance

In this work, we perform mechanical characterization of load-bearing porous biomaterials for bone replacement over their entire design space. Results capture the shift in geometry and mechanical properties between as-designed and as-manufactured biomaterials induced by additive manufacturing. Characterization of this shift is crucial to ensure appropriate manufacturing of bone replacement implants that enable biological fixation through bone ingrowth as well as mechanical property harmonization with the native bone tissue. In addition, we propose a method to include manufacturing imperfections in the numerical models that can reduce the discrepancy between predicted and tested properties. The results give insight into the use of structurally porous biomaterials for the design and additive fabrication of load-bearing implants for bone replacement.

1. Introduction

Metallic porous biomaterials are commonly used as coating in a wide range of clinical applications involving joint replacement surgery. They generally feature high surface area, beneficial to bone ingrowth and biological fixation, as well as an open cell micro-architecture facilitating nutrient transport [1–3]. More recently, porous biomaterials have been also proposed for use in applications that go beyond coatings and require load-bearing capacity. Latest studies have shown that the geometric parameters describing their porous architecture, such as cell topology, nodal

* Corresponding author.
E-mail address: damiano.pasini@mcgill.ca (D. Pasini).

https://doi.org/10.1016/j.actbio.2017.09.013
1742-7061/

connectivity, pore size, and porosity [4–6], can be rationally designed to attain load-bearing capacity beyond that of current porous coatings [7–9]. It has also been demonstrated that tailoring gradients of porosity can augment the functionality of hip replacement implants by reducing bone resorption secondary to stress shielding [10–12].

The ability to fabricate porous biomaterials with a controlled micro-architecture is crucial to the success of bone replacement implants. Traditional methods, such as direct metal foaming and powder metallurgy, can generally produce random pore distribution and non-homogeneous porosity; others, such as vapor deposition, can only produce an almost uniform and homogenous arrangement of cells [3,13]. However, they often provide limited freedom in generating complex geometry, with pore shape and graded pore distribution that can best fulfill specific biological and mechanical requirements. Recent advances in additive manufacturing (AM), such as electron beam melting (EBM) and selective laser melting (SLM), bring versatile layer-by-layer processes that facilitate the fabrication of porous materials and bone replacement implants with controlled pore morphology. Additionally, through AM, gradients of porosity and pore size can be introduced into the micro-architecture to enhance mechano-biological performance with respect to anatomical location [14,15].

Despite the advantages of bone ingrowth and biological fixation offered by current porous coatings and devices, one of their limitations is their lack of strength, a factor that limits their use to coating on a solid substrate and small augments. Their structural performance is poor with strength not sufficiently high to resist the severe cyclic loading certain biomedical implants, such as a hip-replacement, experience during their service life [16–18]. To address this problem, we introduced structurally porous biomaterials with yield strength five times stronger than that of tantalum foam and other commercially available porous coatings [8]. In addition, we showed in a clinical investigation that these biomaterials not only promote bone ingrowth, but also are effective in reducing some of the clinical shortcomings of hip-replacement implants currently available on the market [19]. A strategy developed to elucidate the relation between cell morphology, mechanical properties, bone ingrowth, and manufacturing constraints induced by additive processes was applied to a set of porous biomaterials with cell morphology suitable for bone replacement. Structurally porous biomaterials were fabricated via SLM, mechanically tested, and assessed *in vivo* to investigate their mechano-biological response in bone. We found that in a canine transcortical study, implants made from these biomaterials demonstrated bone ingrowth of $36 \pm 2\%$ and $57 \pm 4\%$ after four and eight weeks respectively.

While extremely promising, that investigation highlighted several challenges that called for further investigation. The first is the clear geometry mismatch between as-designed and as-manufactured biomaterials, a dominant factor in contributing to the mechanics discrepancy observed between predicted and tested properties. Practical use of structurally porous biomaterials for load-bearing implants necessitates the search for a solution. A mismatch in geometry could potentially lead to degradation of pore interconnectivity and permeability. For cell feature size close to the manufacturing limit of AM, this degradation could cause partial or complete pore occlusion, thus preventing bone ingrowth [20–23]. As well, inaccurate predictions of their mechanical properties, such as stiffness and strength, could compromise the fabrication of implants that are mechanically biocompatible, thereby possibly culminating in stress shielding and implant failure [17,24,25].

A second challenge that emerged from our previous study deals with the limited portion of the design space that was examined for mechano-biological characterization [8]. Samples with constant pore size only were investigated with porosity varying from 50% to 75%. However, a full characterization of the design space for porous biomaterials is fundamental to the understanding of the relationship between their mechano-biological properties and their morphological parameters. A third challenge the previous study prompted was the need to quantify the unavoidable geometric and mechanics discrepancies between model predictions and testing results to orientate design choices for bone replacement applications.

The aim of this work is to address the challenges described above via a combination of integrated experiments and computational analysis on fabricated porous biomaterials. First, we explore the entire design space of two porous biomaterials suitable for load-bearing implants and characterize their predicted and actual mechanical properties as a function of their morphological parameters. The investigation is conducted on two high-strength cell topologies, the Tetrahedron-based and Octet-truss [26–28], for which bone ingrowth was clinically demonstrated [8]. Second, to predict more accurately their mechanical behavior, we characterize the geometric shift induced by SLM. We present numerical models with porous architecture statistically similar to their as-built counterpart. Selected AM defects are measured through micro computed tomography (μCT) and their statistical distribution is used to generate predictive models that parallel the behavior of as-manufactured biomaterials. Third, we generate morphological and mechanical maps that characterize the geometric and mechanical property shifts induced by SLM with the goal of providing tools that can assess the mechanical response and guide the design of porous biomaterials.

The article is organized as follows. In Section 2, we perform a design of experiments within the admissible domain for load-bearing implants and we manufacture via SLM 160 titanium alloy (Ti-6Al-4V) porous biomaterials with Tetrahedron-based and Octet-truss unit cells. The samples are morphologically assessed via μCT, mechanically tested in compression, and simulated through finite element analysis (FEA). In Section 3, the results are used to generate characterization maps assessing their mechanical properties and overlaid on their admissible design domain. Finally, in Section 4, we provide clinical context to the results reported in this article by assessing the porous biomaterials performance and comparing their mechanical properties to cortical and cancellous bone as well as other types of porous biomaterials available on the market.

2. Methods

In Section 2.1, we first review the geometry and design space for the two cell topologies of high-strength biomaterials for bone replacement [8]. Section 2.2 details the fabrication of additively manufactured porous biomaterials, while Sections 2.3 and 2.4 delineate the morphological and mechanical investigations, along with the description of the numerical models in Sections 2.5 and 2.6.

2.1. Selection and design of additively manufactured porous biomaterials

Fig. 1 shows the design space for the Tetrahedron-based and Octet-truss cells. These cell topologies have been selected for their stretch-dominated mechanism of deformation, which provides the high structural efficiency necessary to use them as stiff and strong material in load-bearing implants [8,27], and for their cubic symmetry (Fig. A.2 in A), which conveniently reduces to 3 the number of independent constants required to define the elastic stiffness tensor. Recently investigated in the context of biomaterials, these cell topologies were also used to clinically assess bone ingrowth

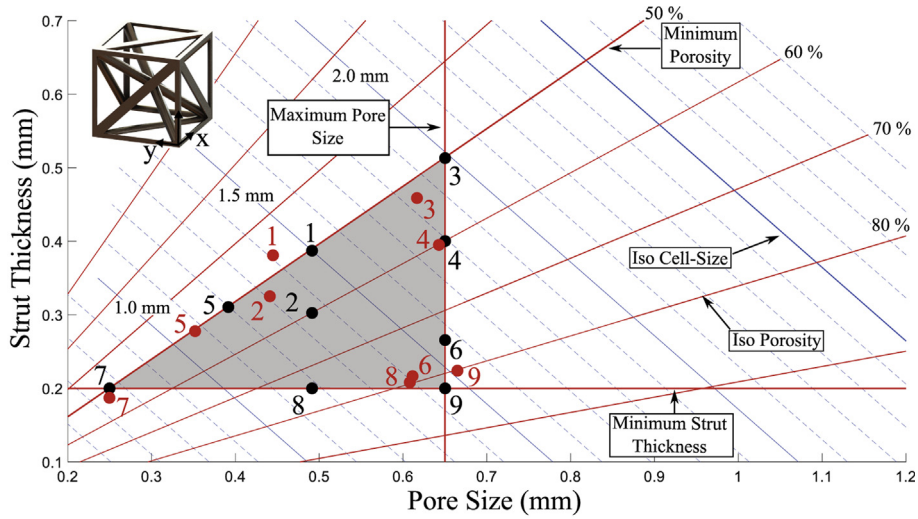

(a) Admissible design space for Tetrahedron-based cell

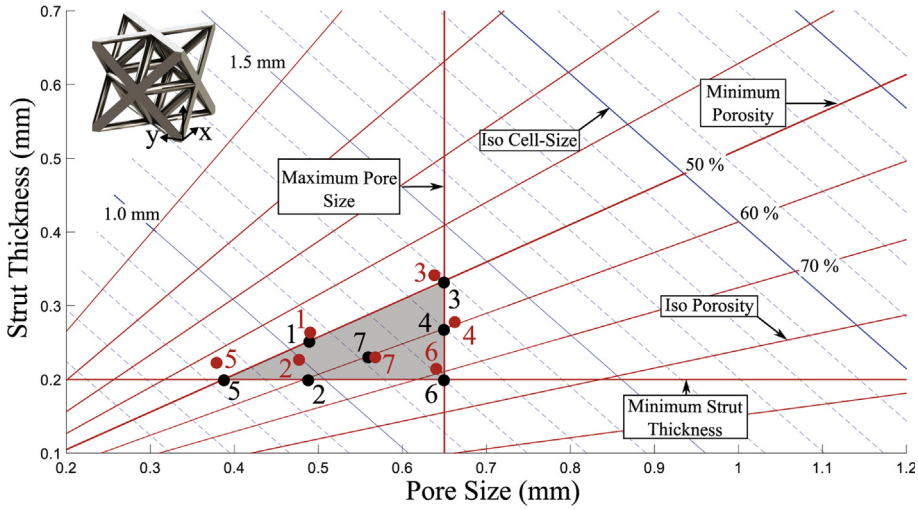

(b) Admissible design space for Octet-truss cell

Fig. 1. Admissible design space for Tetrahedron-based and Octet-truss cells with imposed constraints on manufacturing, pore size, and porosity. Black and red bullets indicate as-designed and as-manufactured unit cells of porous biomaterial samples. (For interpretation of the references to colour in this figure legend, the reader is referred to the web version of this article.)

[8], as well as to develop the first fully porous hip implant that is capable of minimizing bone resorption secondary to stress shielding [19]. To define the admissible design space of each unit cell (Fig. 1), we first plot isometric lines of porosity and cell size with respect to the pore size and the strut thickness. If bone ingrowth requirements (pore size between 50 and 650 μm and porosity higher than 50% [29,30]) along with manufacturing constraints (smallest nominal strut thickness of 200 μm) are specified on the map, a triangular design domain emerges with boundaries and extent that depend on cell topology. For a given cell, the grey area represents values of its geometric parameters that are both manufacturable with respect to the capability of current AM technology and appropriate for osseointegration. Since a main goal of this work is to perform a complete mechanical characterization of their entire design space, we select representative points (in black) at the boundary of the domain (grey) to cover comprehensively its extent. As visualized in Fig. 1 for both cell topologies, the first four points are for porosity of 50% and 60% and pore size of 490 μm and 650 μm (points Tetra #1–4 and Octet #1–4 in Table 1). These points allow for a direct comparison of the effect of cell topology across pore size and porosity with morphological values corresponding to samples used for an *in vivo* bone ingrowth animal model [8]. Given the variation in the admissible design space between the cells, for the larger Tetrahedron-based domain, we further select two points on the bone ingrowth boundaries (point Tetra #5 with porosity of 50% and point Tetra #6 with pore size of 650 μm) and three points on the manufacturing limit boundary (points Tetra #7–9 with strut thickness of 200 μm). For the Octet-truss, which has a smaller design domain, the number of points reduces to seven (Octet #5–6 with strut thickness of 200 μm and Octet #7 in the middle of the design space with porosity of 60%).

For the mechanical investigation here undertaken, we fabricate samples with unit cell features that comply with the ISO 13314 [31] and tessellate each cell in Fig. 1 along the orthonormal directions x, y, and z. 16 porous specimens (9 Tetrahedron-based and 7 Octet-truss lattices) are fabricated with periodicity of $10 \times 10 \times 15$ and geometric details reported in Table 1. The morphological parameters are defined and measured according to the protocol followed in a previous work [8]. The strut thickness corresponds to the diameter of the circular cross-section while the pore size

Table 1
Geometric details of as-designed samples.

Unit cell	#	Porosity (%)	Strut thickness (mm)	Unit cell size (mm)	Pore size (mm)	Height (mm)	Width (mm)	Depth (mm)
Tetrahedron	1	50	0.385	1.50	0.490	22.5	15.0	15.0
	2	60	0.297	1.36	0.490	20.4	13.6	13.6
	3	50	0.500	2.00	0.650	30.0	20.0	20.0
	4	60	0.390	1.80	0.650	27.0	18.0	18.0
	5	50	0.300	1.25	0.390	18.8	12.5	12.5
	6	73	0.265	1.60	0.650	24.0	16.0	16.0
	7	50	0.200	0.78	0.250	15.6	10.1	10.1
	8	75	0.200	1.20	0.490	18.0	12.0	12.0
	9	83	0.200	1.43	0.650	21.5	14.3	14.3
Octet-truss	1	50	0.255	1.08	0.490	16.1	10.8	10.8
	2	60	0.200	0.98	0.490	16.7	10.8	10.8
	3	50	0.340	1.41	0.650	21.1	14.1	14.1
	4	60	0.278	1.32	0.650	19.8	13.2	13.2
	5	50	0.200	0.83	0.390	15.0	10.0	10.0
	6	73	0.200	1.21	0.650	18.1	12.1	12.1
	7	60	0.235	1.13	0.560	16.9	11.3	11.3

is defined as the diameter of the largest inscribed sphere that can pass through neighboring cells. This definition of pore size reflects cell interconnectivity [32], which has a large influence on bone ingrowth [6]. The porosity is measured via a parametric numerical model of the two cell topologies and represents the percentage of void in a fully solid cube bounding the cell.

Fig. 1 captures the geometric boundary of each unit cell and serves as a baseline in Section 3 to generate morphological and mechanical maps for as-designed and as-built porous biomaterials. Each map is generated with the least squares method from the experimental and computational data obtained for each sample. Second-order models are used to interpolate the manufacturing performance and the mechanical behavior throughout the admissible domains. Further details on the response surface methodology are given in Appendix B.

2.2. Sample manufacturing

16 selected geometries are built in 10 replicates via SLM out of Ti-6Al-4V alloy (Renishaw AM-250) with powder size ranging from 15 to 50 μm. This additive process uses a 200 W laser with energy density of 60 J/mm^3 and spot diameter of 70 μm. All samples are fabricated with point by point exposure at intervals of 30 μm layer thickness on a titanium base plate. To reduce the level of interstitial elements that can react with Ti-6Al-4V powder (e.g. Nitrogen, Carbon, Hydrogen and Oxygen), the build chamber is flushed with Argon gas. To enhance mechanical properties, the samples are annealed at 730 °C for 2 h. While heat treatment does impact the mechanical properties, it has been demonstrated that its effect on the morphological parameters is negligible [33]. Hence, the effect of heat treatment on the morphological parameters is neglected in this study. Following heat treatment, the specimens are removed from the build plate with electrical discharge machining. The mechanical properties of the solid material are provided by our manufacturer following tensile test of standard specimens with laser parameters identical to those used to build the porous biomaterial samples of this work [34,35].

2.3. Morphological investigation

A representative sample of each design point is scanned using a SkyScan 1172 high-resolution μCT to investigate SLM fidelity in rendering cell morphology. The representative sample is selected with respect to the average manufacturing error following weighting and measuring the porous biomaterials. During the μCT analysis, each sample is rotated from 0° to 360° and 5 images are recorded at each increment of 5°. To measure pore size and strut thickness, we reconstruct the μCT data into cross-sectional images using NRecon (Skyscap N.V., Kontich, Belgium). The reconstruction process includes lower and upper thresholds of 80 and 255, ring artifact reduction of 4, and beam-hardening correction of 40%.

2.4. Compression testing

All 160 manufactured lattices are tested in compression on a 50 kN MTS servo-electric machine with a constant strain rate of 0.01 s^{-1}. For each reference set, 5 samples are first tested to failure to retrieve the full stress-strain curve, which displays the first maximum and the plateau strengths. The remaining 5 samples are tested in the linear regime to obtain their compressive elastic modulus along the building direction (z-axis) as per the ISO-13314 standard [31]. The strain is measured with an extensometer mounted on the samples. The value of the elastic modulus is then used on the full stress-strain curves to identify the yield strength at 0.2% offset from the linear elastic response. The mechanical maps generated with the experimental results use as input the mean values of the tested properties. To offer a statistical context to the experimental data, the standard deviation of the results is provided in Appendix C.

2.5. Finite element analysis of as-designed models

To compare the predicted and tested mechanical properties of the as-built 3D samples, we perform finite element analysis (FEA) on ideal as-designed lattices using the commercial software package ABAQUS (Dassault Systemes Simulia Corp, France). Because of the high thickness ratio of the struts (defined as the thickness over the length), ranging from 0.140 to 0.256, Euler-Bernoulli and Timoshenko beam theory assumptions do not hold here [36]. Thus, the numerical models generated in this work use ten-node tetrahedral elements (C3D10) with isotropic material properties of 3D-printed Ti-6Al-4V that underwent heat treatment (E = 114 GPa, $\nu = 0.342$) [34]. In the linear regime, Asymptotic Homogenization (AH) is applied to a representative volume element (RVE) of a given sample to compute the complete stiffness tensor E_{ijkl}, from which the effective elastic modulus in the corresponding loading direction is extracted [10,37]. A detailed description of this method is given in Appendix C. To calculate the yield strength, we did not resort to AH as it is done for the elastic properties. AH underestimates the yield strength since the yield strength is defined as the macro stress at which the first element

reaches the yield point of the base material. Rather, we conducted detailed finite simulations on a reduced order lattice with x, y, and z periodicity ensuring results convergence (see Appendix A). The values obtained numerically were then validated experimentally. In the numerical calculations, the base material (additively manufactured Ti-6Al-4V) was assumed to be isotropic with linear elastic perfectly-plastic behavior according to the shape of its stress and strain curve [38] with constitutive relationship described by J2 flow theory (von Mises). The bulk properties of Ti-6Al-4V were obtained from a set of tests of dog-bone samples fabricated with laser processing and heat treatment parameters identical to those used to build the porous biomaterial samples of this work. The yield strength of the base material ($\sigma_y = 1120$ MPa) represents the average from the yield strength measured along the building direction (996 MPa) and perpendicular to the building direction (1145 MPa). Rigid and frictionless properties were defined for the edge-to-edge contact between the structural struts. A smooth step displacement-controlled loading was applied to obtain the numerical stress and strain curve. Rigid body movements were removed by applying a symmetry constraint on the top and bottom planes of the lattice. The yield strength was measured on the numerical stress-strain curve with the 0.2% offset method (see above Section 2.4) as detailed in the ISO 13314 standard [31]. See Appendix C for more details about the mechanical properties characterization.

2.6. Generation of imperfect-geometry models and simulations

The mechanical properties of as-designed models fail to capture the actual response of the as-built 3D porous biomaterials under compression. To create numerical models that better predict their mechanical properties, we investigate a set of SLM defects that typically emerge during manufacturing. Fig. 2 shows the full μCT-reconstructed Octet #6 lattice with a close-up on one unit cell. The design lines (red) overlaid on the reconstructed unit cell highlight a clear discrepancy between as-designed and as-manufactured cell geometry. Fig. 2 also displays scanning electron microscopy (SEM) images of the Octet #6 sample illustrating the imperfect geometry of the struts rendered during SLM. Among the observable defects, two imperfections that are most relevant here are highlighted: (1) irregular geometric profile of a strut, discernible as variation of cross-sectional shape along the strut axis (Fig. 2-B), and (2) center axis deviation from the principal axis of an ideal strut (Fig. 2-**C**). To account for these geometric defects into the numerical models, we reconstruct from μCT images representative sets of struts, classified based on their orientation with respect to the SLM build plane. The Tetrahedron-based cell exhibits 3 orientations (horizontal, vertical, and diagonal), whereas the Octet cell features 2 orientations (horizontal and diagonal). As described in Appendix D, the geometry of each strut is extracted as a surface mesh and sectioned with a series of parallel planes perpendicular to the ideal strut axis (Fig. D.1)). The effective radius of a circle fitted through the points on each plane and the offset of the center of this circle with respect to the ideal axis of the strut are determined and used to construct probability distributions of each geometric imperfection. In turn, each probability distribution is fitted to a probability density function using a Kernel density estimation. This process enables the generation of numerical data (strut thickness and center deviation) that follow geometric imperfection distributions. Fig. D.2 presents the smoothed probability density distributions. The results are used via an in-house code to generate numerical models with imperfect porous architecture that is statistically equivalent to that of their as-manufactured counterpart (Fig. D.3)). The method of including manufacturing defects into numerical models is computationally efficient and recent work has shown its potential to predict accurately the mechanical behavior of lattices built with SLM [39]. Further details on the generation of imperfect models are given in Appendix D.

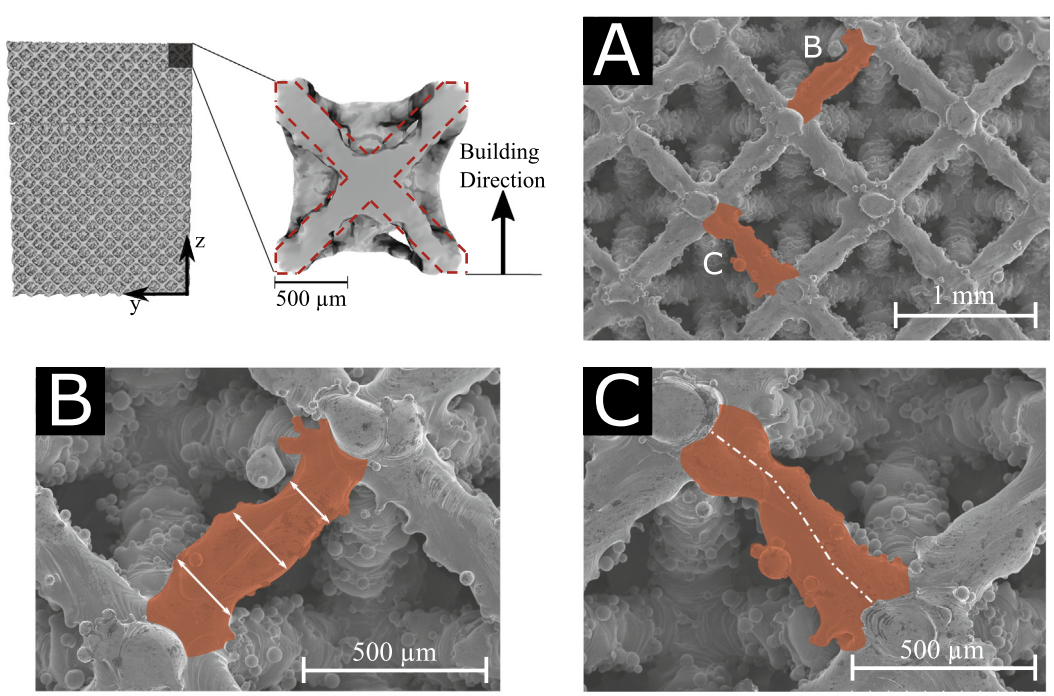

Fig. 2. μCT-reconstructed Octet #6 sample with close up on one unit cell. Top-left: hidden lines (red) overlaid on reconstructed unit cell represent as-designed geometry. SEM images with SLM manufacturing defects highlighted for Octet #6: non-uniform cross-sectional shape and thickness (**B**) and center deviation of the strut axis (**C**). (For interpretation of the references to colour in this figure legend, the reader is referred to the web version of this article.)

2.7. Statistical analysis

To compare as-designed (FEA on as-designed geometry) and experimental results, a two-tailed t-test is performed. The null hypothesis is expressed as:

$$H_0 : \mu_{Exp} = X_{Design}, \quad (1)$$

where μ_{Exp} is the mean of the experimental results and X_{Design} the as-designed value. Similarly, a two-tailed t-test is conducted to compare experimental results with FEA results from the imperfect-geometry model. For this case, the null hypothesis is expressed as:

$$H_0 : \mu_{Exp} = \mu_{Imperfect}, \quad (2)$$

where $\mu_{Imperfect}$ is the mean of the FEA results on the imperfect-geometry model. The p-values are reported in Table C.2 with significance level set at $p < 0.05$.

3. Results

3.1. Morphology of porous biomaterials

Porosity, pore size, and strut thickness, which are among the main morphological parameters of a porous biomaterial, are measured from μCT images and compared to their respective design values listed in Table 1. Fig. 3 presents a set of maps characterizing the structural geometry of the porous biomaterials under investigation. Relative errors for pore size, porosity, and strut thickness between as-designed and as-manufactured values are visualized for both cell topologies. Expressed in percentage, the relative error of a given geometric parameter is defined as the difference between the measured and nominal value, normalized by the measured value here assumed as baseline. Besides the maps for porosity, pore size, and strut thickness, Fig. 3 also displays the overall manufacturing error, calculated as the arithmetic mean error of the three morphological parameters.

The results in Fig. 3a show an average manufacturing error of 6.2% for the Tetrahedron cell with an increase of the error toward the manufacturing limit of 200 μm for the strut thickness. While the porosity error (maximum of 7.7%) is almost uniform throughout the domain, the pore size and strut thickness maps display local regions in the admissible design space with higher relative error. The design set #8 (Fig. 1), which lies on the manufacturing constraint boundary and has a nominal pore size of 490 μm, features the highest pore size error of 18% which can be attributed to unformed horizontal struts revealed by μCT images. In addition, the strut thickness error in Fig. 3a highlights a maximum of 15% accuracy error for samples with the highest design porosity of 83%.

While the Tetrahedron-based topology exhibits relatively low and uniform morphological errors, with peaks of geometry mismatch associated with local regions, Fig. 3b shows that, for the Octet-truss topology, the manufacturing error increases with smaller feature size (cell size and strut thickness). The response surface of the porosity error in Fig. 3b demonstrates this trend, as the error increases from 1.9% to 23% for unit cell size of 1.41 mm to 0.83 mm and strut thickness of 340 μm to 200 μm. For the design set #5 (Fig. 1), which has the smallest nominal cell size of 830 μm, the stringent geometric requirements combined with the shortcomings of SLM to reproduce accurately small features led to a manufactured sample with lower porosity (41% ± 6%) compared to its as-designed counterpart (50%).

3.2. Mechanical properties

Fig. 4 shows the mechanical property maps for the compressive elastic modulus of the Tetrahedron-based and Octet-truss unit cells, each obtained from the experimental and numerical results of both as-designed and imperfect-geometry models. In particular, response surfaces of the elastic modulus are presented for the as-designed (upper-left corner), experimental (upper-right corner), and imperfect-geometry model (bottom-left corner). The elastic modulus is normalized by the elastic modulus of fully solid titanium alloy (E = 114 GPa). The fourth map at the bottom right corner illustrates the difference between the experimental and imperfect-geometry model elastic moduli, normalized by their respective experimental values.

For the as-designed Tetrahedron-based lattices, Fig. 4a shows a decrease of the compressive elastic modulus from 17% to 3.2% for porosity of 50% to 83%. The experimental response surface at the upper-right corner also shows a relationship between elastic modulus and porosity but displays smaller compressive stiffness. The most significant reduction of the elastic modulus occurs for Tetra #2 ($E_{Design}/E_{Ti6Al4V} = 10.1\%$, $E_{Exp}/E_{Ti6Al4V} = 7.9\% \pm 0.3\%$, p-value < 0.001) and Tetra #4 ($E_{Design}/E_{Ti6Al4V} = 10.0\%$, $E_{Exp}/E_{Ti6Al4V} = 7.3\% \pm 0.8\%$, p-value = 0.0013). The maximum as-manufactured elastic modulus is also smaller than its as-design counterpart ($E_{Design}/E_{Ti6Al4V} = 16.8\%$, $E_{Exp}/E_{Ti6Al4V} = 12.3\% \pm 0.9\%$, p-value < 0.001). The results for the elastic modulus obtained from the imperfect-geometry model are reasonably accurate with an average error of 11% from the experimental results. The trends in Fig. 4a also parallel those from the experiments. Quantitatively, the difference between the experimental and imperfect elastic moduli, shown in the fourth response surface, ranges from 5.4% to 19%. The error increases with porosity, reaching its highest value at the highest as-designed porosity of 83% where the manufacturing error peaks (Fig. 3a).

Similar to the Tetrahedron-based lattices, Fig. 4b shows the as-designed elastic modulus for the Octet-truss topology which varies with porosity, ranging from 6.3% to 21% for porosity of 75% to 50%. In addition, the as-designed values are stiffer than the experimental elastic modulus, the latter ranging from 3% ± 2% (p-value = 0.0128) to 15% ± 1% (p-value < 0.001). However, for high porosity, the response surface of the experimental elastic modulus exhibits a variation of the elastic modulus with pore size. The imperfect-geometry model captures this trend and predicts the elastic modulus of the Octet-truss lattices with an average accuracy error of 12%.

Fig. 5 shows mechanical characterization maps for the compressive yield strength. Here, the values are normalized by the yield strength of the fully solid titanium alloy (S_Y = 880 MPa) [33]. The last response surface (bottom-right corner) plots the difference between the experimental and imperfect yield strengths, normalized by the experimental value.

For the Tetrahedron topology in Fig. 5a, the as-designed yield strength varies from 3.8% to 21% with porosity of 83% to 50%. The response surface of the experimental yield strength displays smaller values, ranging from 1.5% ± 0.2% (p-value < 0.001) to 17% ± 2% (p-value = 0.0126). The imperfections included in the numerical model enable accurate prediction of the yield strength. This is confirmed by the imperfect-geometry model map that reveals an average error between predicted and tested yield strength of 10% (fourth response surface at bottom-right corner in Fig. 5a).

Fig. 5b presents the yield strength maps for the Octet-truss topology. Governed by porosity, the as-designed yield strength varies from 8.4% to 24%. Similar to the compressive elastic modulus, the yield strength of the built lattices displays a dependency on the pore size at higher porosity and ranges from 4.7% ± 0.4% to 20.7% ± 0.8%. The imperfect numerical model satisfactorily succeeds in predicting the mechanical behavior of the as-manufactured samples with an error that varies from 1.9% to 9.9% for the Octet-truss topology with an average error of 4.5%.

The maps in Figs. 4 and 5 highlight the mismatch between mechanical properties of the ideal geometry models and the

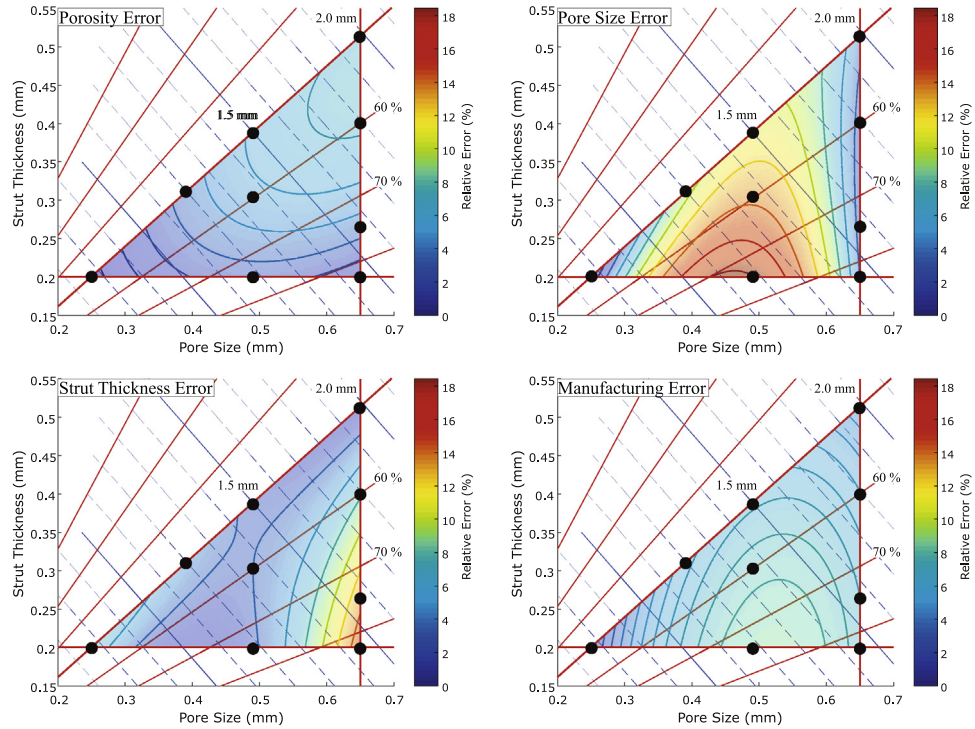

(a) Tetrahedron-based cell

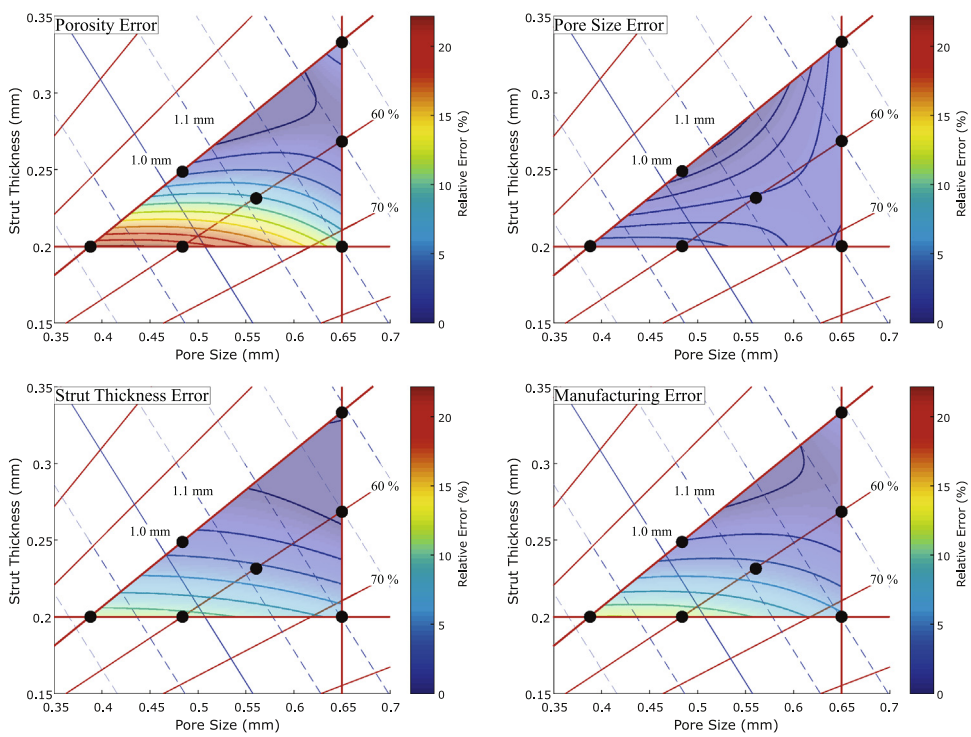

(b) Octet-truss cell

Fig. 3. Morphological maps of the error between as-designed and as-manufactured morphological parameters. The fourth map (lower right corner) represents the manufacturing error, i.e., the average of the porosity, pore size, and strut thickness errors.

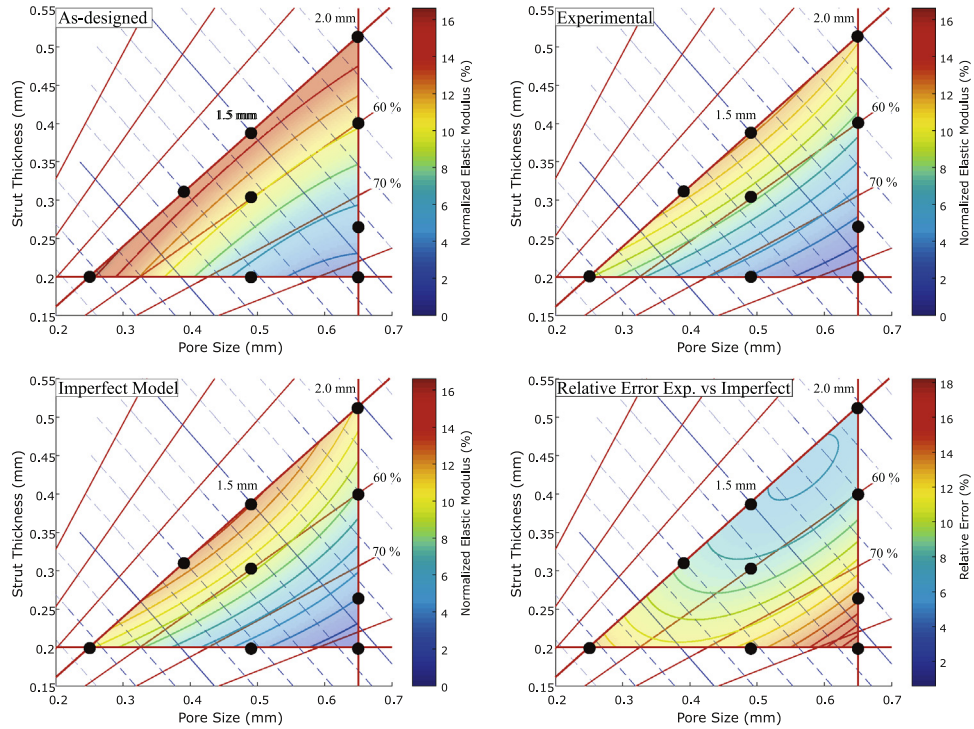

(a) Tetrahedron-based cell

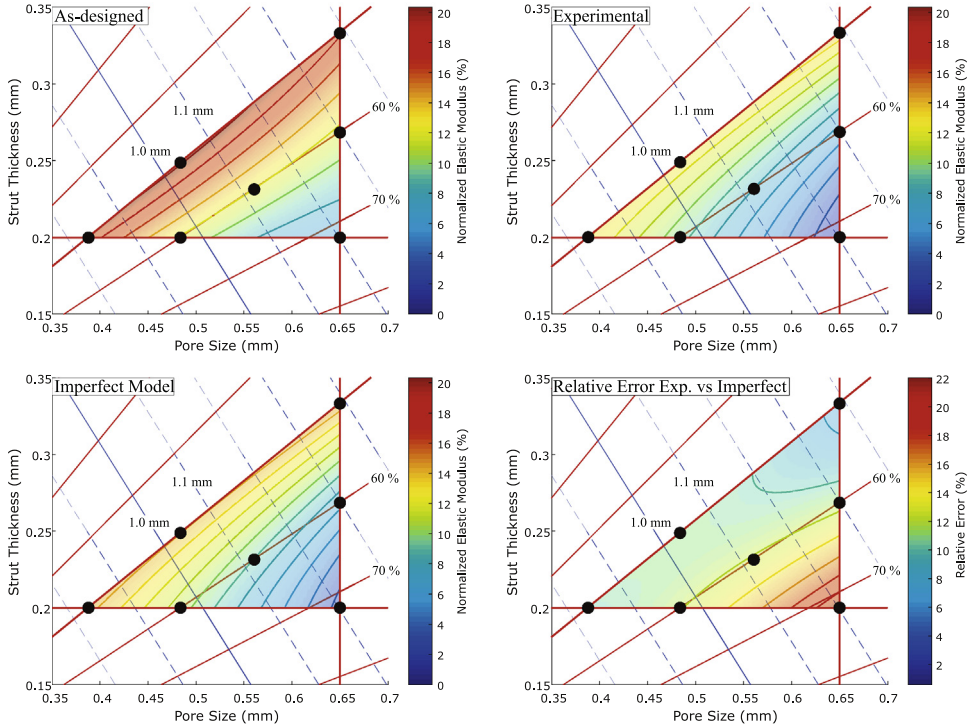

(b) Octet-truss cell

Fig. 4. Elastic modulus maps obtained from experiments, as-designed model, and imperfect-geometry model. The fourth response surface (lower right corner) illustrates the relative error between the imperfect-geometry predicted and experimentally measured elastic modulus.

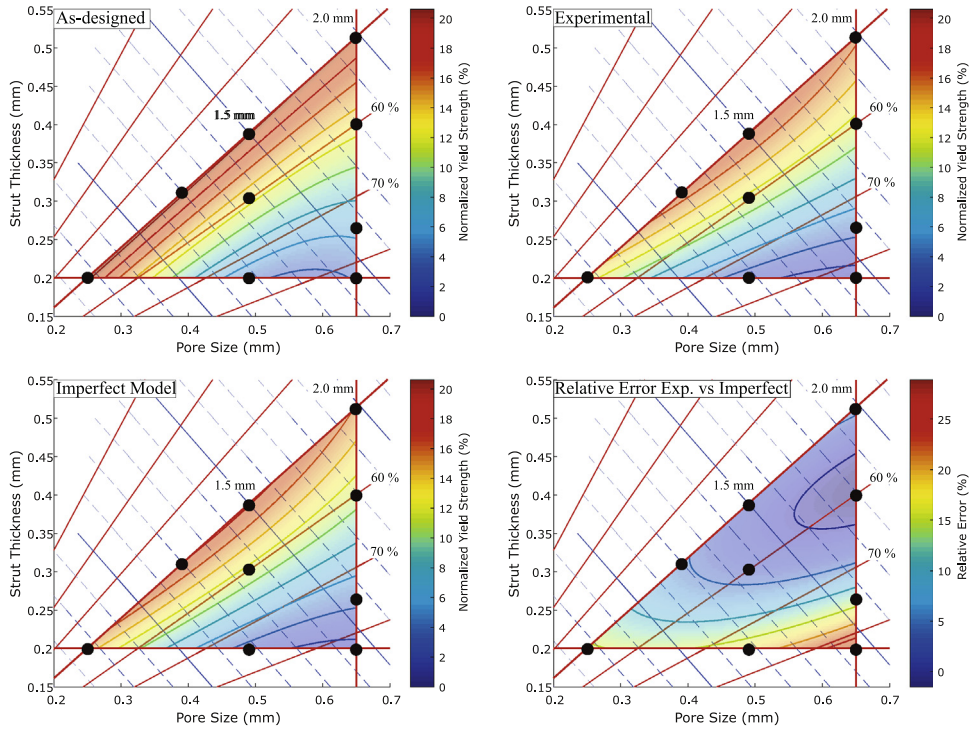

(a) Tetrahedron-based cell

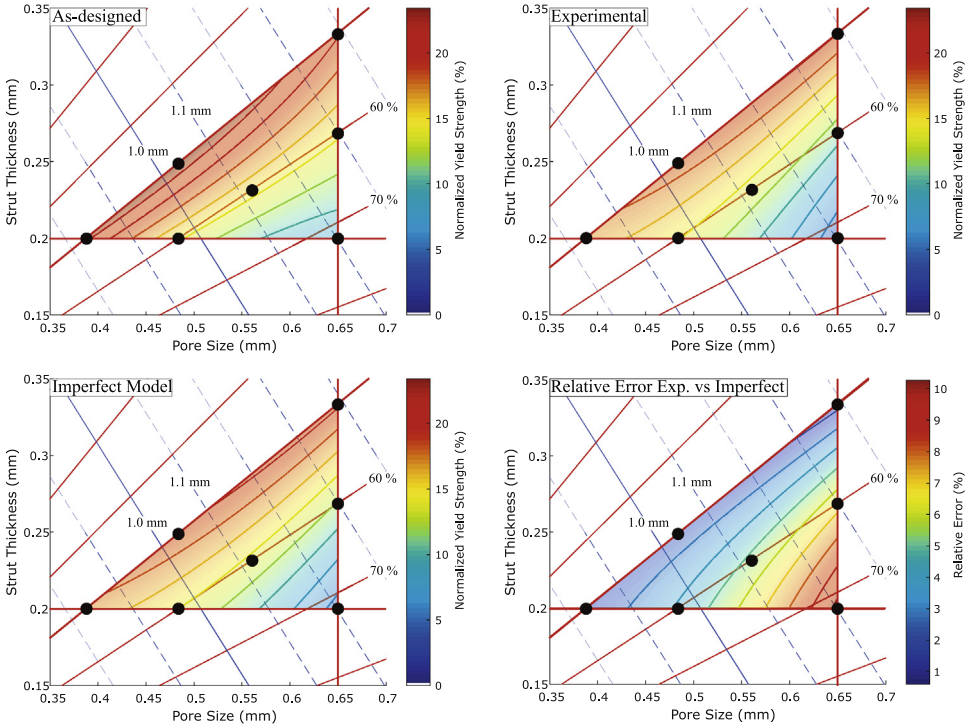

(b) Octet-truss cell

Fig. 5. Yield strength maps obtained from experiments, as-designed model, and imperfect-geometry model. The fourth response surface (lower right corner) depicts the relative error between the imperfect-geometry predicted and experimentally measured yield strength.

as-built porous biomaterials. The reduction of this mismatch is achieved by generating imperfect-geometry models with probability distributions of SLM imperfections. Using this scheme, for the elastic modulus, the average error with the tested elastic modulus reduces from 42% (as-designed) to 11% (imperfect-geometry) for the Tetrahedron-based cell and from 57% (as-designed) to 12% (imperfect-geometry) for the Octet-truss cell. Similarly, the average mismatch with the tested yield strength reduces from 51% (as-designed) to 10% (imperfect-geometry) and from 27% (as-designed) to 4.5% (imperfect-geometry) respectively for the Tetrahedron-based and Octet-truss cells.

4. Discussion

4.1. Comparison to prior studies

In a recent study showing the potential of additively manufactured porous biomaterials for load-bearing applications, we have highlighted challenges for their use in orthopaedics [8]. One of these challenges pertains to the geometric discrepancy between as-designed and as-manufactured porous biomaterials. In this work, a comprehensive morphological and mechanical characterization of two high-strength cell topologies has been performed to assess the impact geometric induced imperfections play on the mechanical properties of porous biomaterials. Given some manufacturing defects caused by AM cannot currently be mitigated, we have developed a methodology that can incorporate geometric imperfections in the numerical models. The results show a strong reduction of the error between predicted and tested properties. The scheme here presented enables a more accurate appraisal of the mechano-biological performance of additively manufactured porous biomaterials for arthroplasty, especially for load-bearing implants.

Several studies have corroborated the suitability of additively manufactured porous titanium alloy for orthopaedic applications [7,40,41]. From a mechanical point of view, these studies considered porosity as the main parameter governing stiffness and strength of porous biomaterials, thereby reaching the conclusion that for stretch-dominated cell topologies these properties scale linearly with relative density (ρ), as predicted by theoretical models [27,42,43]. Supporting this claim, Pattanayak et al. [44] studied porous titanium implants generated from CT scans of human trabecular bone and reported an increase in the compressive strength from 35 MPa to 120 MPa with a decrease in porosity from 75% to 55%. Similarly, Murr et al. [7] investigated the effect of varying the structural features of a unit cell on the compressive elastic modulus of porous titanium and identified a reduction from 1.03 GPa to 0.58 GPa with porosity varying between 59% and 88%. While porosity has a great influence on the mechanical properties, more recent studies have exposed the influence of other morphological parameters on the mechanical properties. Parthasarathy et al. [9] evaluated the effect of pore size, strut size, and porosity on the mechanical properties of porous titanium samples built by EBM. Compression testing revealed that not only porosity, but also strut thickness has an influence on the elastic modulus and compressive strength. In another study investigating SLM manufactured samples with fixed topology and porosity, Yan [45] recorded a reduction of stiffness and strength with larger cell sizes. Parthasarathy and Yan's results illustrate the limitations of using porosity alone to predict the mechanical properties of additively manufactured porous biomaterials. Despite extensive research on the mechanical characterization of porous titanium, no work has so far explored the combined role all morphological parameters play on the behavior of porous biomaterials within the admissible requirements for bone ingrowth.

Other studies have considered the effects of manufacturing imperfections in a computational framework, where the variation of strut cross-section is accounted for in the numerical model [39,46,47]. Ravari et al. [46] demonstrated a reduction of the error between predicted and tested mechanical properties from 127.9% to 6.1% for a sample with given parameters of beam and solid elements. For a wide range of porosity, Campoli et al. [47] modeled variable cross-section as well as heterogeneous porosity of struts to reduce the errors between predicted and tested elastic properties. In our work, we further explore the impact of other manufacturing imperfections. More specifically, besides non-uniform cross-section, center axis deviation (Fig. 2) of as-manufactured struts is included in the numerical models. Developed in a previous work for beam elements [39], the scheme is here applied to solid elements with error reduction for the elastic modulus from 42.0% to 4.0% and for compressive strength from 47.2% to 12.7%. This work thus put forward a systematic strategy that can explain, predict, and reduce geometric and mechanics mismatches between as-designed and as-manufactured porous biomaterials.

4.2. Clinical implications: geometric mismatch

For cementless orthopaedic implants, bone formation is a critical requirement that depends not only on exogenous factors (the properties of the implanted material), but also on endogenous factors controlled by the characteristics and regenerative capability of the host bone [48]. In this work, we focus on the influence of morphological parameters of porous biomaterials that are relevant to bone ingrowth. For a periodic porous biomaterial, rational design of porosity, pore size, and pore interconnectivity can bolster bone ingrowth through perfusion and transport of osteoinductive factors, such as cells, proteins, and genes [1–3,17]. For example, pore sizes must first respect the known dimensions that have been shown to clinically ensure osseointegration in an acceptable time frame [20,21]. Second, careful adjustment of pore distribution must be performed to enhance permeability. This is critically important to enable vascular invasion and the supply of nutrients and growth factors required for osseointegration [22,23]. The results in Section 3 of this investigation highlight a clear geometry mismatch between as-designed and as-manufactured porous biomaterials with maximum deviation of 23.4%, 22.5%, and 21.7% for porosity, pore size, and strut thickness, respectively. This geometry mismatch, specific to the SLM parameters used for this work, could be even more important for as-designed geometry beyond the current capacity of additive manufacturing technology. Van Bael et al. reported maximum manufacturing errors of 25%, 45% and 116% for their porous biomaterials with large as-designed pore size (500–1000 μm) and extremely thin as-designed strut thickness (100 μm) [49].

As depicted in Fig. 6, this discrepancy induces a shift of the admissible design domains. By joining the points corresponding to the average morphological parameters of the additively manufactured biomaterials taken from Table C.1, qualitative manufacturing domains emerge for the Tetrahedron-based and Octet-truss cells and overlay those of the as-designed geometry. For both topologies, Fig. 6 illustrates regions of the design spaces that could not be built, as evident for the Octet-truss domain close to the current manufacturing limit for strut thickness (200 μm). In addition, the manufacturing domains (red) for both topologies show regions outside of the admissible design domains (grey). This could have an important clinical impact on the implant's performance since biomaterials with a low porosity and a high pore size have less bone ingrowth and the ingrowth can take longer to occur [50,51]. The problem may accrue when the element size gets close to the manufacturing limits, because manufacturing imperfections can lead to complete pore occlusion. Our study proposes a

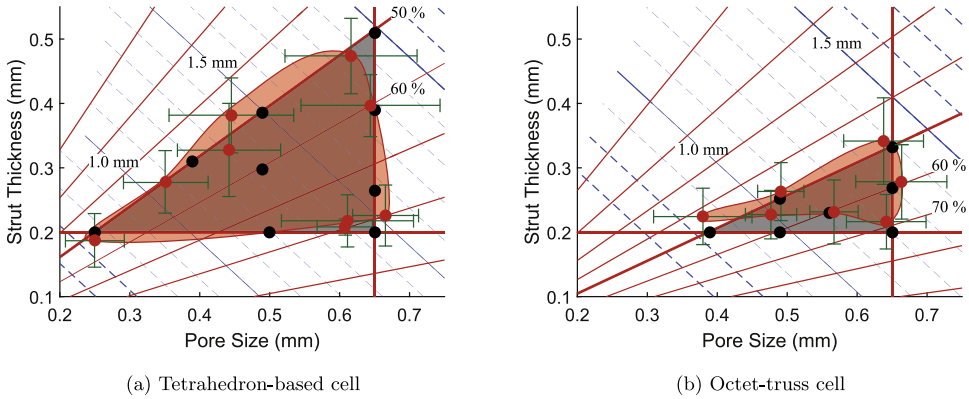

(a) Tetrahedron-based cell (b) Octet-truss cell

Fig. 6. As-designed and as-manufactured spaces of the additively manufactured porous biomaterials unveiling a geometric shift caused by SLM imperfections. The error bars represent the standard deviations of the as-manufactured pore size and strut thickness listed in Table C.1.

methodological scheme that gives insight into that geometric shift so as to avoid the design of implants in regions where morphological parameters fall outside of the admissible design domain. For example, if porosity of 50% along with pore size of 390 μm are required for an orthopaedic implant with Octet-truss topology, Fig. 6 shows the current limits of SLM in achieving this value (50%) with manufactured porosity of 41% ± 6%. This manufacturing error could lead to an implant with sub-optimal mechano-biological performance.

The geometry shift can be mitigated to a certain extent through different approaches, such as design strategies, machine parameter tuning, or post-processing techniques. In a recent study [52], we developed a design strategy to compensate the design of lattice materials by correlating the as-produced thickness to the angle a strut forms with the building plane. This scheme allows for a reduction of strut thickness error from 17% to 6.5%. On the other hand, through another approach that aims at tuning machine parameters, Qiu et al. [53] investigated the effect of changing SLM parameters, mainly laser power and laser speed, on the quality of several morphological features including strut thickness and porosity. Despite the success of these studies, there is an inherent limitation on the resolution current AM technology can achieve. Hence the methodology here presented aims at taking into account current shortcomings so as to bridge the gap between predicted and tested properties of porous biomaterials.

4.3. Clinical implications: mechanical property mismatch

Recent studies have shown that mechanical biocompatibility between an orthopaedic implant and the surrounding bone tissue can be assured if there is iso-elasticity between the two interfacial components [10,11]. An implant with an effective stiffness close to that of the surrounding tissue promotes load transfer and alleviates stress shielding [17,24,25]. Fig. 7a reports the as-designed effective elastic modulus of the Tetrahedron-based and Octet-truss cells on a material property chart. For porosity varying between 50 and 83%, the range of elastic modulus for the Tetrahedron-based cell (3–19 GPa) and Octet-truss (7–24 GPa) can cover the elastic modulus range of cortical bone and penetrate the spectrum of cancellous bone. This enables the tuning of elastic modulus to levels that match bone properties, resulting in cell morphology that ensures satisfactory bone ingrowth and reduces stress shielding. As expected for stretch-dominated topology, the elastic modulus of as-designed porous biomaterials scales with the relative density as depicted in Fig. 7a by the line of constant E/ρ. Compared to fully dense titanium with elastic modulus of 114 GPa, the porous biomaterials have a high potential to have their porosity tuned to match the properties of the surrounding native bone. Fig. 7a compares the results of the structurally porous biomaterials herein presented with other commercially available porous biomaterials used for coating [5,54–57]. Trabecular metal (Zimmer Biomet), with porosity varying from 75% to 85%, exhibits an elastic modulus ranging from 2.5 to 4.0 GPa [58]. GRIPTION (Johnson & Johnson Medical Limited) is made of sintered titanium beads with 63% average porosity and 0.86 GPa elastic modulus [59,60]. Finally, the additively manufactured Tritanium (Stryker) has an elastic modulus equal to 6.2 GPa for an average porosity of 60% [61]. All porous biomaterials available in the market have bend-dominated architecture and Fig. 7a reveals their reduced structural efficiency compared to the structural porous biomaterials introduced in this work.

Fig. 7a also depicts the mechanical shift between as-designed and as-manufactured biomaterials. As discussed in Section 3, both cell topologies display a lower elastic modulus after fabrication, ranging from 2 to 14 GPa for the Tetrahedron-based cell, and from 7 to 16 GPa for the Octet-truss. While the manufactured Tetraheron-based biomaterial displays a similar scaling law to its as-designed counterpart, the manufactured Octet-truss biomaterial highlights a variation of its slope for lower relative density, i.e. for higher porosity, which results in reduced specific stiffness. This trend is observed in Fig. 4a for the experimental response surface of the Octet-truss biomaterial and can be attributed to an increase of manufacturing imperfections at high porosity. Broken and unformed struts, as well as partial pore occlusion, found in our μCT investigation, can induce local change in the deformation mechanism of the unit cell. This leads to cells that are neither purely stretch-dominated nor bend-dominated, but a in hybrid state of deformation, thus resulting in a dissimilar scaling law of the elastic modulus.

With respect to the yield strength, the structurally porous biomaterials here investigated show much higher values than the porous biomaterials currently available on the market. As a result, these biomaterials have a load-bearing capability which allows them to be used for orthopaedic implants that are required to withstand severe cyclic loading. Fig. 7b shows the yield strength of the as-designed and as-manufactured biomaterials in a classical material property chart. Similar to the elastic modulus, the compressive yield strength of the as-designed implants (23–193 MPa for the Tetrahedron-based and 23–212 MPa for the Octet-truss cell) scales approximately with the constant line of σ_y/ρ (Fig. 7b). The biomaterials as-designed yield strength is higher than their as-manufactured counterpart (13–151 MPa for the Tetrahedron-based and 42–182 MPa for the Octet-truss cell). As shown in Section 3 and highlighted again in Fig. 7b, the scaling law of the yield strength shifts at high porosity for the as-manufactured biomaterials. This could be attributed to manufacturing defects of SLM rendering a micro-architecture

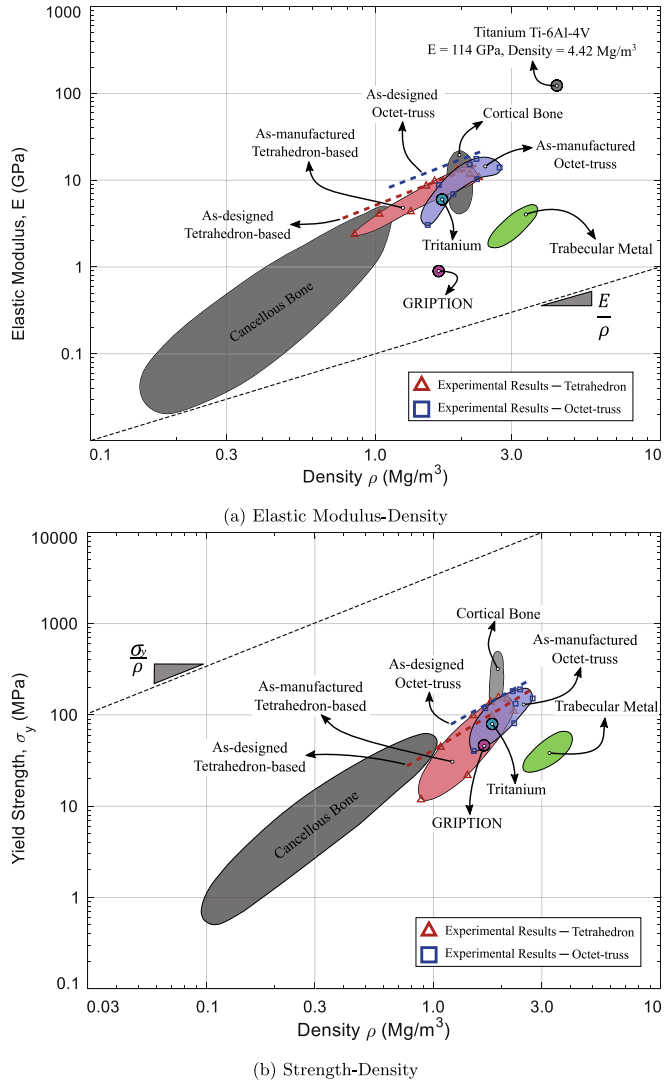

Fig. 7. Material property charts comparing the mechanical properties of struturally porous biomaterials with Tetrahedron-based (red) and Octet-truss (blue) topology to other commercially available biomaterials: Trabecular metal (green), GRIPTION (pink), and Tritanium (turquoise). The mechanical properties of the FE as-designed models, represented by hidden lines, follow the scaling laws for stretch-dominated cell topologies ($\frac{E}{\rho}$ and $\frac{\sigma_y}{\rho}$). The experimental results, represented by geometric symbols, are used to generate domains for as-manufactured mechanical properties showing different scaling laws, especially at high porosity. (For interpretation of the references to colour in this figure legend, the reader is referred to the web version of this article.)

with non-uniform strut thickness along its length, non-circular cross-section shape, mass agglomeration at the joints, and surface roughness caused by attached beads of un-melted powder. In addition, the strength of other porous biomaterials commercially available is presented in Fig. 7b. The yield strength of trabecular metal ranges from 35 to 51 MPa [59], while the yield strength of GRIPTION and Tritanium is respectively 32 MPa and 85 MPa [60,61]. The yield strength of Tritanium is calculated at the average porosity based on the typical scaling law characterizing bend-dominated cellular materials. All competing porous biomaterials available in the market shown in Fig. 7b exhibit yield strength lower than the structurally porous biomaterials presented in this study.

Illustrated in Fig. 7, the mechanical mismatch between predicted and tested properties is also reported by several other authors. For porous scaffolds with nominal porosity around 50% and cell size of 2 mm, Dias et al. [62] reported a post-manufactured elastic modulus 18–38% lower than the as-designed value. For the Octet-truss cell, Liu et al. [39] obtained a difference of 42.0% and 47.2% between as-designed and as-manufactured elastic modulus and compressive strength. Their additively manufactured sample had a porosity of 85.3% and a cell size of 3 mm. On the other hand, with comparable cell size and strut thickness of 100 μm, Van Bael et al. [49] reported lower errors between predicted and tested properties, averaging 11%. However, these results need to be evaluated with care since the as-built struts were 113% thicker than their nominal values, thus resulting in as-manufactured samples stiffer and stronger than their as-designed counterparts. Our investigation, along with the above studies, confirms the challenge of manufacturing porous biomaterials with small features using additive manufacturing.

While Fig. 7 compares the mechanical properties of the structurally porous biomaterials presented in this work to other biomaterials available on the orthopaedic market, other studies have proposed different cell topologies for bone replacement implants. Cheng et al. fabricated Ti-6Al-4V high porosity samples (62%–92%) with stochastic architecture (e.g. foam) and reticulated mesh [63]. Similarly to our biomaterials, they showed tunability of material properties with elastic modulus varying from 0.2 to 6.3 GPa and compressive strength varying from 4 to 113 MPa. The cubic unit cells fabricated by Parthasarathy et al. offers an elastic modulus of 0.57–2.92 GPa and a compressive strength of 7.28–163.02 MPa for a porosity of 50% and different strut thicknesses [9]. Although these cells show high compressive strength and elastic modulus within the range of bone, they are all bend-dominated and they were all tested on small samples with no clinical assessment so far reported on their bone ingrowth. The structurally porous biomaterials that we present in this work exhibit larger range of elastic moduli (2–17 GPa) and higher compressive strength (up to 182 MPa for 50% porosity). While other cell topologies, such as triply periodic minimal surfaces, can achieve even higher strength [64], in the current study, we focus on porous architecture, for which bone ingrowth was demonstrated *in vivo* in canine models [8], and which was used to engineer a fully porous femoral stem that can reduce stress shielding [19].

4.4. Addressing potential limitations

This work has focused on metallic porous biomaterials with high structural efficiency fabricated with additive processes. We have studied their mechanical properties via a combined approach of computations and experiments, and developed design maps that show a mismatch in geometry and mechanical properties between as-designed and as-manufactured biomaterials. The maps in Figs. 4 and 5 illustrate the homogenized mechanical properties of structurally porous biomaterials. They represent the effective properties of an unbounded periodic cellular domain with unit cell size at least one order of magnitude below the length scale of the macro domain. They can thus be used to design bone replacement implants. Local deformations, on the other hand, are not investigated in this study since they are highly dependent on the implant macro geometry. Yet in the design of an implant, it is critical to determine local stresses that result from physiological loads applied to the implant so as to ensure proper implant fixation [65]. Although the focus has been on two main sources of defects—strut thickness variation and strut center axis deviation—others also play a role in the mechanics and biological performance of porous biomaterials. We refer to the mass agglomeration at the nodes, broken or unformed struts, and surface roughness caused by the beads of un-melted powder, defects that can be included in the imperfect-geometry models with a scheme similar to what is here presented. Further work is also required to complement the maps presented here with others describing bone

ingrowth, permeability, and other metrics characterizing the biological performance of additively manufactured porous biomaterials. Finally, while this work investigates the material response to quasi-static compression, other loading scenarios should be studied to warrant the use of structurally porous biomaterials in orthopaedics. Cyclic loading is especially relevant to bone replacement implants, and is critical to understand the fatigue behavior of biomaterials. A recent study on additively manufactured porous biomaterials has highlighted a close relationship between fatigue strength and the amount of tensile stress generated in the unit cells [66]. In particular, it has been shown that for cubic cells, a global compression induces internal compression only at the micro-scale, a phenomenon that results in remarkably high fatigue strength to yield strength ratio. For the stretch-dominated cells examined in this work, on the other hand, tensile stress can appear in the cells, thereby potentially reducing their fatigue resistance; hence further work is needed to study their response under cyclic load.

5. Conclusions

The success of a load-bearing implant depends to a large extent on its ability to promote osseointegration and to emulate the mechanical behavior of bone. Implant fixation through bone ingrowth, mechanical biocompatibility, and biologic performance are important requirements to satisfy. In this work, we have focused on the relationship between biomaterial microarchitecture and mechanical properties, and discussed their potential impact on the biological performance of load-bearing implants. Through a combination of experiments and simulations, we have presented morphological and mechanical property maps of two high-strength biomaterials, for which bone ingrowth was previously demonstrated *in vivo*. The morphological maps capture the distinct geometry shift between as-designed and as-manufactured biomaterials, with maximum manufacturing discrepancy of 23.4%, 22.5%, and 21.7% for porosity, pore size, and strut thickness, respectively. The mechanical property maps also show the potential for these materials to have their stiffness tuned to match that of the native bone, and their strength bolstered for load-bearing applications. The obtainable range of elastic modulus varies from 3.7–24 GPA (as-designed) to 2–16 GPa (as-manufactured) and the obtainable range of yield strength varies from 33.3–212 MPa (as-designed) to 13–182 MPa (as-manufactured). These maps characterize the entire admissible domain for bone replacement implants, giving insight into the difference between simulated and tested models as a function of the morphological parameters of the unit cell. Altogether, these geometric and mechanical mismatches have severe influence on the implant success: the former could lead to pore occlusion that would limit bone ingrowth, and the latter could result in a biomaterial with stiffness outside of the range of cortical and cancellous bone, thereby falling short of the maximum achievable performance. The design maps and numerical models integrating statistical based imperfections presented in this article enable visualization and prediction of the property shifts induced by additive manufacturing. The methodological scheme proposed in this investigation succeeds in reducing the error between predicted and tested mechanical properties from 49% to 11% (elastic modulus) and 41% to 7.6% (yield strength). This work provides robust design tools for bone replacement biomaterials.

Acknowledgements

The authors acknowledge the financial support from the Natural Sciences and Engineering Research Council of Canada (NSERC) and the Canadian Institutes of Health Research (CIHR).

Appendix A. Mechanical characterization details

A.1. Asymptotic homogenization

The biomaterials presented in this work have x, y, and z periodicity of $10 \times 10 \times 15$. This corresponds to 1500 unit cells, 23,705 struts for the Tetrahedron-based topology, and 27,800 struts for the Octet-truss topology. Full scale finite element analysis on such complex models is computationally expensive. Instead, here we computed the effective elastic modulus by analyzing a representative region of the biomaterial, the representative volume element (RVE). The biomaterial is therefore replaced by an equivalent homogeneous solid with effective properties. In this work, we performed asymptotic homogenization to solve the following local problem defined on the RVE [67,68]:

$$\int_{Y_C} E_{ijpm}\varepsilon^1_{ij}(v)\varepsilon^{*kl}_{pm}(u)dY = \int_{Y_C} E_{ijkl}\varepsilon^1_{ij}(v)\bar{\varepsilon}_{kl}dY, \tag{A.1}$$

where $\varepsilon^1_{ij}(v)$ is the virtual strain, $\varepsilon^{*kl}_{pm}(u)$ is the microstructural strain corresponding to the component kl of the macroscopic strain tensor $\bar{\varepsilon}_{kl}$, Y_C is the solid part of the cell, and E_{ijkl} is the local stiffness tensor. To maintain the periodicity of the field quantities, we impose periodic boundary conditions on the RVE by setting equal the displacement on opposite edges [68,69]. Assuming small deformation and elastic material behavior, the solution of equation (A.1) unfolds a linear relation between the macroscopic ($\bar{\varepsilon}_{ij}$) and microscopic (ε_{ij}) strains:

$$\varepsilon_{ij} = M_{ijkl}\bar{\varepsilon}_{kl}. \tag{A.2}$$

The local structural tensor M_{ijkl} is given as follow:

$$M_{ijkl} = \frac{1}{2}(\delta_{ik}\delta_{jl} + \delta_{il}\delta_{jk}) - \varepsilon^{*kl}_{ij}, \tag{A.3}$$

where δ_{ij} is the Kronecker delta. For the three-dimensional case, we apply six independent unit strains to construct the M_{ijkl} matrix. Finally, the effective stiffness tensor is computed according to the following equation, where $|Y|$ is the volume of the entire unit cell:

$$E^H_{ijkl} = \frac{1}{|Y|}\int_{Y_C} E_{ijpm}M_{pmkl}dY, \tag{A.4}$$

The elastic modulus along the biomaterial loading direction (reported in this work) is obtained from the stiffness tensor given by Eq. (A.4).

A.2. Polar plot of the elastic modulus

The effective stiffness tensor E^H_{ijkl} obtained from asymptotic homogenization is expressed in the cartesian coordinate system (x, y, z). A new orthogonal coordinate system $(x\prime, y\prime, z\prime)$ can be created with $z\prime$-axis parallel to the original z-axis, and $x\prime$-axis oriented at an angle θ counterclockwise. This transformation is shown in Fig. A.1.

The rotation matrix of this transformation is:

$$[L_\theta] = \begin{bmatrix} \cos\theta & \sin\theta & 0 \\ -\sin\theta & \cos\theta & 0 \\ 0 & 0 & 1 \end{bmatrix} \tag{A.5}$$

The stress tensor in the new coordinate system is expressed as:

$$[\sigma\prime] = [L_\theta][\sigma][L_\theta]^T. \tag{A.6}$$

Using Voigt notation, Eq. (A.6) can be written as:

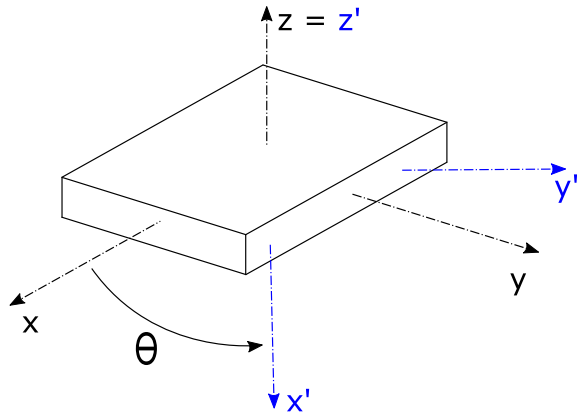

Fig. A.1. Transformation of stress and strain components of a material defined in two different coordinate systems.

$$[\sigma\prime] = [M_\sigma][\sigma], \tag{A.7}$$

$$\begin{bmatrix} \sigma_{xx}\prime \\ \sigma_{yy}\prime \\ \sigma_{zz}\prime \\ \sigma_{yz}\prime \\ \sigma_{xz}\prime \\ \sigma_{xy}\prime \end{bmatrix} = \begin{bmatrix} \cos^2\theta & \sin^2\theta & 0 & 0 & 0 & \sin 2\theta \\ \sin^2\theta & \cos^2\theta & 0 & 0 & 0 & -\sin 2\theta \\ 0 & 0 & 1 & 0 & 0 & 0 \\ 0 & 0 & 0 & \cos\theta & -\sin\theta & 0 \\ 0 & 0 & 0 & \sin\theta & \cos\theta & 0 \\ -\frac{1}{2}\sin^2\theta & \frac{1}{2}\sin^2\theta & 0 & 0 & 0 & \cos 2\theta \end{bmatrix} \begin{bmatrix} \sigma_{xx} \\ \sigma_{yy} \\ \sigma_{zz} \\ \sigma_{yz} \\ \sigma_{xz} \\ \sigma_{xy} \end{bmatrix} \tag{A.8}$$

Similarly, we can express the strain tensor as:

$$[\varepsilon\prime] = [M_\varepsilon][\varepsilon], \tag{A.9}$$

$$\begin{bmatrix} \varepsilon_{xx}\prime \\ \varepsilon_{yy}\prime \\ \varepsilon_{zz}\prime \\ 2\varepsilon_{yz}\prime \\ 2\varepsilon_{xz}\prime \\ 2\varepsilon_{xy}\prime \end{bmatrix} = \begin{bmatrix} \cos^2\theta & \sin^2\theta & 0 & 0 & 0 & \sin\theta\cos\theta \\ \sin^2\theta & \cos^2\theta & 0 & 0 & 0 & -\sin\theta\cos\theta \\ 0 & 0 & 1 & 0 & 0 & 0 \\ 0 & 0 & 0 & \cos\theta & -\sin\theta & 0 \\ 0 & 0 & 0 & \sin\theta & \cos\theta & 0 \\ -\sin^2\theta & \sin^2\theta & 0 & 0 & 0 & \cos 2\theta \end{bmatrix} \begin{bmatrix} \varepsilon_{xx} \\ \varepsilon_{yy} \\ \varepsilon_{zz} \\ 2\varepsilon_{yz} \\ 2\varepsilon_{xz} \\ 2\varepsilon_{xy} \end{bmatrix} \tag{A.10}$$

In the reference system (x, y, z), Hookes's law is expressed:

$$[\sigma] = [E^H][\varepsilon]. \tag{A.11}$$

In the new system $(x\prime, y\prime, z\prime)$, Hookes's law yields the following equation:

$$[\sigma\prime] = [M_\sigma][E^H][M_\varepsilon]^T[\varepsilon\prime], \tag{A.12}$$

from which the effective stiffness matrix in the new configuration $[E^H\prime]$ can be expressed as:

$$[E^H\prime] = [M_\sigma][E^H][M_\varepsilon]^T. \tag{A.13}$$

The effective compliance matrix $[S^H\prime]$ is the inverse of the stiffness matrix $[E^H\prime]$ and the elastic modulus along the $x\prime$-axis can be written as:

$$E\prime_{xx} = \frac{1}{S^H_{11}\prime}. \tag{A.14}$$

Changing the rotational angle θ from 0° to 360°, we can generate a polar plot of the elastic modulus along the $x\prime$-axis as shown in Fig. A.2.

Applying the same procedure, we can generate the polar plot of the elastic modulus on the x-z and y-z planes. Fig. A.2 shows that the tetrahedron and octet-truss have cubic symmetry, with the latter showing nearly isotropic material properties.

A.3. Numerical yield strength calculation

To calculate the yield strength of the structurally porous biomaterials, we did not resort to AH as this technique defines the yield strength as the macro stress at which the first element reaches the yield point of the base material. This approach is conservative as it underestimates the yield strength. For this reason, we conducted detailed finite simulations on a reduced order lattice with x, y, and z periodicity ensuring results convergence. In the numerical calculations, the base material (additively manufactured Ti-6Al-4V) was assumed to be isotropic with linear elastic perfectly-plastic behavior according to the shape of its stress and strain curve [38] with constitutive relationship described by J2 flow theory (von Mises). The bulk properties of Ti-6Al-4V were obtained from a set of tests of dog-bone samples fabricated with laser processing and heat treatment parameters identical to those used to build the porous biomaterial samples of this work. The yield strength of the base material ($\sigma_y = 1120$ MPa) represents the average from the yield strength measured along the building direction (996 MPa) and perpendicular to the building direction (1145 MPa). Rigid and frictionless properties were defined for the edge-to-edge contact between the structural struts. A smooth step

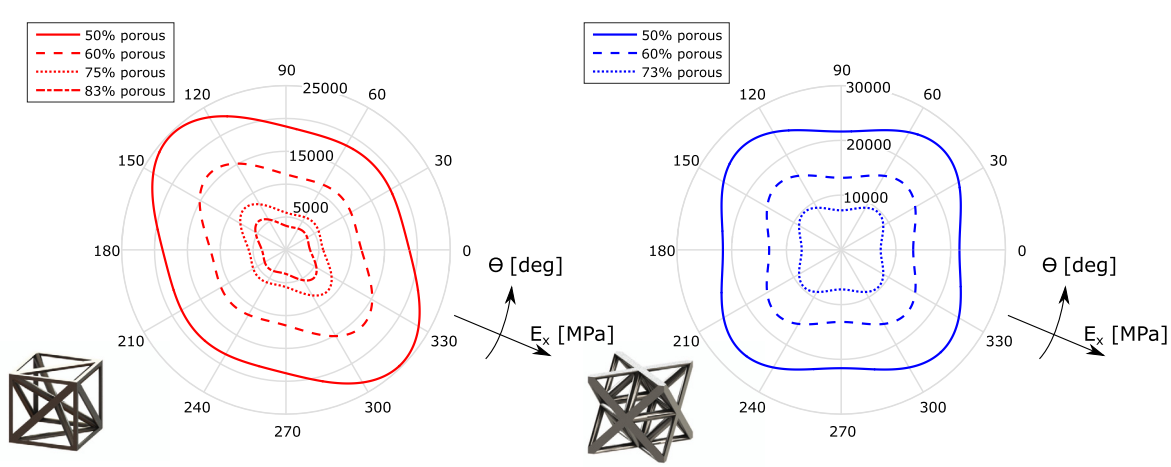

Fig. A.2. Polar plot of the elastic modulus along the x-axis for the as-designed Tetrahedron-based and Octet-truss cells.

displacement-controlled loading was applied to obtain the numerical stress and strain curve. Rigid body movements were removed by applying a symmetry constraint on the top and bottom planes of the lattice. The yield strength was measured on the numerical stress-strain curve with the 0.2% offset method as detailed in the standard ISO 13314 [31].

Appendix B. Response surface methodology

For many engineering applications, the relationship between true response of a system (y) and a set of predictor variables $(x_1, x_2, \ldots, x_k)$ can be unknown or not known exactly. Such relationship can be expressed as a multiple linear regression model which can be written as:

$$y = \beta_0 + \beta_1 x_1 + \beta_2 x_2 + \cdots + \beta_k x_k + \varepsilon, \tag{B.1}$$

where y is the true response variable and the parameters $\beta_j, j = 0, 1, \ldots, k$, are called the regression coefficients. This model spans a k-dimensional space defined by the regressor $\{x_j\}$. The parameter ε is the error of the regression model.

To provide a continuous approximation of the true response, in this work, we use response surface methodology to generate the morphological and mechanical property maps. First, we perform a design of experiments in the admissible domain for bone replacement biomaterials to allow the generation of second-order models in two variables. These models are expressed as follows:

$$y = \beta_0 + \beta_1 x_1 + \beta_2 x_2 + \beta_{11} x_1^2 + \beta_{22} x_2^2 + \beta_{12} x_1 x_2 + \varepsilon, \tag{B.2}$$

where y is the true property of the biomaterials, x_1 the pore size, and x_2 the strut thickness. If we let $x_3 = x_1^2,\ x_4 = x_2^2,\ x_5 = x_1 x_2$, $\beta_3 = \beta_{11},\ \beta_4 = \beta_{22}$, and $\beta_5 = \beta_{12}$, we can write Eq. (B.2) in the general form of a multiple linear regression model in Eq. (B.1).

To estimate the regression coefficients β_j, we use the method of least squares. The model Eq. (B.1) can be written in matrix notation as:

$$\mathbf{y} = \mathbf{X}\beta + \boldsymbol{\varepsilon}, \tag{B.3}$$

where:

$$\mathbf{y} = \begin{bmatrix} y_1 \\ y_2 \\ \vdots \\ y_n \end{bmatrix},\ \mathbf{X} = \begin{bmatrix} 1 & x_{11} & x_{12} & \cdots & x_{1k} \\ 1 & x_{21} & x_{22} & \cdots & x_{2k} \\ \vdots & \vdots & & \vdots & \\ 1 & x_{n1} & x_{n2} & \cdots & x_{nk} \end{bmatrix},\ \beta = \begin{bmatrix} \beta_0 \\ \beta_1 \\ \vdots \\ \beta_k \end{bmatrix},\ \text{and}\ \varepsilon = \begin{bmatrix} \varepsilon_1 \\ \varepsilon_2 \\ \vdots \\ \varepsilon_n \end{bmatrix},$$

Since the goal is to find the regression coefficient vector β that minimizes the error vector ε, we can write the least squares functions as:

$$L = \sum_{i=1}^{n} \varepsilon_i^2 = \varepsilon^T \varepsilon = (\mathbf{y} - \mathbf{X}\beta)^T (\mathbf{y} - \mathbf{X}\beta). \tag{B.4}$$

Eq. (B.4) can be further developed to obtain:

$$L = \mathbf{y}^T\mathbf{y} - 2\beta^T\mathbf{X}^T\mathbf{y} + \beta^T\mathbf{X}^T\mathbf{X}\beta. \tag{B.5}$$

The least squares estimators $b_0, b_1, \cdots, b_k$ must satisfy:

$$\left.\frac{\partial L}{\partial \beta}\right|_{\mathbf{b}} = -2\mathbf{X}^T\mathbf{y} + 2\mathbf{X}^T\mathbf{X}\mathbf{b} = \mathbf{0}. \tag{B.6}$$

Eq. (B.6) simplifies to the normal equations in matrix form:

$$\mathbf{X}^T\mathbf{X}\mathbf{b} = \mathbf{X}^T\mathbf{y}. \tag{B.7}$$

Solving the normal equations gives the least squares estimator $\mathbf{b}$ of the regression coefficients β:

$$\mathbf{b} = \left(\mathbf{X}^T\mathbf{X}\right)^{-1}\mathbf{X}^T\mathbf{y}. \tag{B.8}$$

Hence, the fitted regression model is:

$$\hat{\mathbf{y}} = \mathbf{X}\mathbf{b}. \tag{B.9}$$

The residuals are:

$$\mathbf{e} = \mathbf{y} - \hat{\mathbf{y}}. \tag{B.10}$$

The coefficient of determination is:

$$R^2 = \frac{SS_R}{SS_T} = 1 - \frac{SS_E}{SS_T}. \tag{B.11}$$

The sum of squares of the regression SS_R, the sum of squares of the residual SS_E, and the total sum of squares are:

$$SS_R = \mathbf{b}^T\mathbf{X}^T\mathbf{y} - \frac{\left(\sum_{i=1}^{n} y_i\right)}{n}, \tag{B.12}$$

$$SS_E = \mathbf{e}^T\mathbf{e} = \mathbf{y}^T\mathbf{y} - \mathbf{b}^T\mathbf{X}^T\mathbf{y}, \tag{B.13}$$

$$SS_T = SS_R + SS_E. \tag{B.14}$$

To generate the property maps presented in this paper, we use Eq. (B.9) and discretize the admissible design domains shown in Fig. 1. To validate the response surface methodology and give a statistical background to the maps, we present in Table B.1 their coefficients of determination.

Table B.1
Response surfaces coefficients of determination.

Unit cell	Response surface	Reference figure	Coefficient of determination (R^2)
Tetrahedron	Porosity error	Fig. 3a	0.841
	Pore size error	Fig. 3a	0.856
	Strut thickness error	Fig. 3a	0.322
	Manufacturing error	Fig. 3a	0.439
	As-designed E	Fig. 4a	0.989
	Experimental E	Fig. 4a	0.962
	Imperfect model E	Fig. 4a	0.957
	Exp vs.Imperfect E	Fig. 4a	0.670
	As-designed S_Y	Fig. 5a	0.982
	Experimental S_Y	Fig. 5a	0.988
	Imperfect model S_Y	Fig. 5a	0.979
	Exp vs.Imperfect S_Y	Fig. 5a	0.960
Octet-truss	Porosity error	Fig. 3b	0.946
	Pore size error	Fig. 3b	0.983
	Strut thickness error	Fig. 3b	0.936
	Manufacturing error	Fig. 3b	0.942
	As-designed E	Fig. 4b	0.992
	Experimental E	Fig. 4b	0.924
	Imperfect model E	Fig. 4b	0.945
	Exp vs.Imperfect E	Fig. 4b	0.831
	As-designed S_Y	Fig. 5b	0.999
	Experimental S_Y	Fig. 5b	0.979
	Imperfect model S_Y	Fig. 5b	0.981
	Exp vs.Imperfect S_Y	Fig. 5b	0.958

Appendix C. Experimental data

All response surfaces shown in this work are generated from the analysis of the morphological and mechanical results of 160 manufactured porous samples. Table C.1 lists the morphological parameters obtained via μCT, where μ and σ represent respectively mean and standard deviation. The strut thickness is categorized by its orientation with respect to the building plane. Similarly, Table C.2 details the mechanical properties of the experimental samples, the as-designed models, and the imperfect-geometry models.

Table C.1
Experimental results of the morphological characterization.

Unit cell	#	Porosity [%]		Pore Size [mm]		Strut thickness [mm]					
						0 °		45 °		90 °	
		μ	σ	μ	σ	μ	σ	μ	σ	μ	σ
Tetrahedron	1	52.7	0.8	0.45	0.09	0.40	0.06	0.36	0.07	0.38	0.04
	2	58	4	0.44	0.08	0.42	0.05	0.33	0.04	0.18	0.03
	3	54.2	0.4	0.6	0.1	0.47	0.06	0.46	0.07	0.48	0.04
	4	64.1	0.6	0.6	0.1	0.40	0.05	0.40	0.05	0.40	0.05
	5	52.9	0.7	0.35	0.06	0.27	0.04	0.30	0.05	0.27	0.06
	6	77	1	0.6	0.1	0.22	0.03	0.22	0.05	0.21	0.04
	7	50	7	0.25	0.04	0.19	0.04	0.18	0.04	0.19	0.04
	8	73	3	0.61	0.04	–	–	0.22	0.02	0.20	0.02
	9	82	2	0.67	0.05	0.23	0.06	0.23	0.04	0.22	0.05
Octet-truss	1	48	2	0.49	0.03	0.28	0.04	0.25	0.05	–	–
	2	49	5	0.48	0.04	0.23	0.03	0.23	0.04	–	–
	3	48	1	0.64	0.06	0.34	0.09	0.35	0.05	–	–
	4	61	2	0.66	0.07	0.28	0.06	0.28	0.05	–	–
	5	41	6	0.38	0.07	0.23	0.05	0.22	0.04	–	–
	6	66	2	0.64	0.06	0.22	0.04	0.21	0.05	–	–
	7	58	3	0.57	0.04	0.24	0.05	0.23	0.05	–	–

Table C.2
Numerical and experimental results of the mechanical characterization

Unit Cell	#	Elastic Modulus [GPa]								Yield Strength [MPa]							
		Design (D)		Exp (E)		Imperfect (I)		p-values		Design (D)		Exp (E)		Imperfect (I)		p-values	
		μ	σ	μ	σ	μ	σ	D vs. E	I vs. E	μ	σ	μ	σ	μ	σ	D vs. E	I vs. E
Tetrahedron	1	18.0	–	12	2	13.4	0.3	0.0291	0.111	178	–	146	12	145	18	0.0040	0.914
	2	11.5	–	9.0	0.3	9	1	< 0.001	0.619	121	–	101	2	98	12	< 0.001	0.719
	3	17.1	–	13	2	12	1	0.0084	0.566	164	–	141	18	136	6	0.0386	0.546
	4	11.4	–	8.3	0.9	9.3	0.7	0.0013	0.103	110	–	98	9	96	17	0.0438	0.908
	5	15.4	–	14	1	16	2	0.0746	0.230	158	–	151	17	163	17	0.4347	0.415
	6	5.6	–	3.9	0.7	3.5	0.2	0.0063	0.214	48.5	–	35	5	32	5	0.0039	0.401
	7	19.2	–	10	3	11	1	0.0071	0.429	184	–	112	8	128	10	0.0043	0.115
	8	5.7	–	4.2	0.5	4.8	0.9	0.0113	0.287	33.3	–	22	8	25	8	0.1244	0.603
	9	3.7	–	2	1	2.9	0.4	0.1803	0.383	43.6	–	13	2	17	4	< 0.001	0.041
Octet-truss	1	23.8	–	15	2	16.7	0.2	0.0041	0.277	212	–	181	22	184	13	0.0341	0.852
	2	13.2	–	11	2	12	2	0.0522	0.277	127	–	137	34	134	6	0.6367	0.831
	3	21.6	–	16	1	17.6	0.8	0.0011	0.219	182	–	182	7	185	16	0.9442	0.747
	4	14.2	–	9	1	10	1	0.0017	0.232	136	–	116	13	122	2	0.1201	0.498
	5	21.6	–	14	5	16	2	0.1415	0.607	194	–	144	11	148	6	0.0145	0.582
	6	7.2	–	3	2	4.1	0.8	0.0126	0.390	73.9	–	41.6	3	46	3	< 0.001	0.128
	7	14.0	–	8.1	0.9	9	2	0.0001	0.317	128	–	93.5	13	101	38	0.0039	0.697

Appendix D. Imperfect-geometry model generation

This section details the generation process of the numerical imperfect model with porous architecture that is statistically equivalent to that of their as-manufactured counterpart. Fig. D.1 explains how the manufacturing imperfections are quantified. From the μCT-reconstructed model, the surface mesh of struts is used to measure the effective radius and center axis deviation.

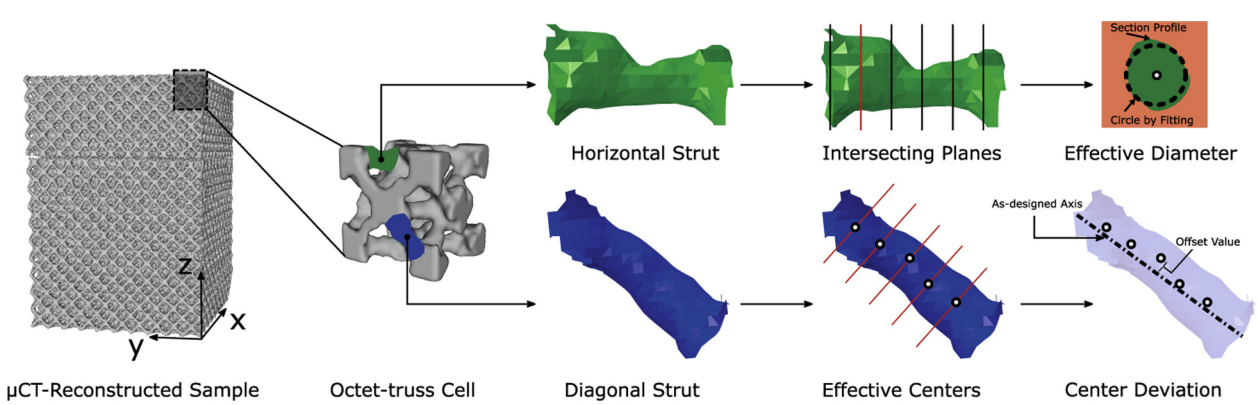

Fig. D.1. Schematic of the process to quantify manufacturing imperfections (Octet #6 selected here as example).

We separate the struts based on their building orientation, as shown in Fig. D.1 for a representative horizontal and diagonal strut of the Octet-truss topology. The Tetrahedron-based topology has vertical, diagonal, and horizontal struts with respect to the building plane. The struts are sectioned with intersecting planes perpendicular to the as-design axis and the nodes lying on this plane are used to fit a circle that minimizes the error with the cross-section profile. The diameter of the circle is defined as the as-manufactured strut thickness that changes along its length. Once the center of the circle of each plane has been calculated, we can obtain the offset value of this center with the as-design axis of the struts. This offset is defined as the as-manufactured center axis deviation.

Once we quantify the struts imperfections, we construct probability distributions of the thickness and the center axis offset. In turn, each probability distribution is fitted to a probability density

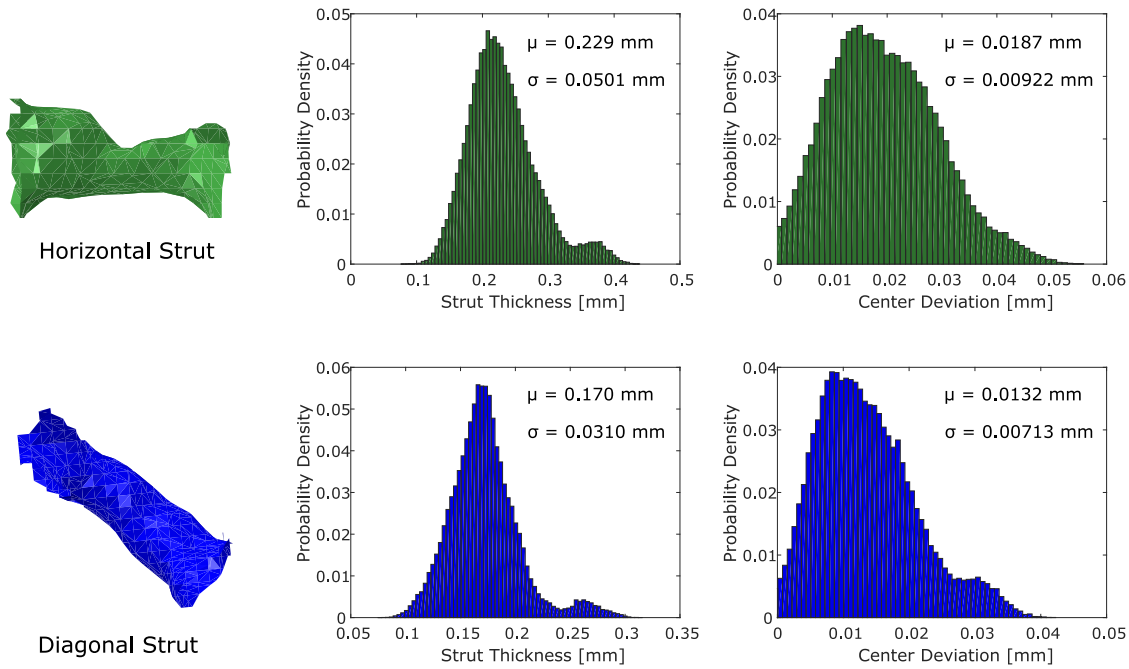

Fig. D.2. Smoothed probability density distributions of strut thickness and center deviation for the Octet #6.

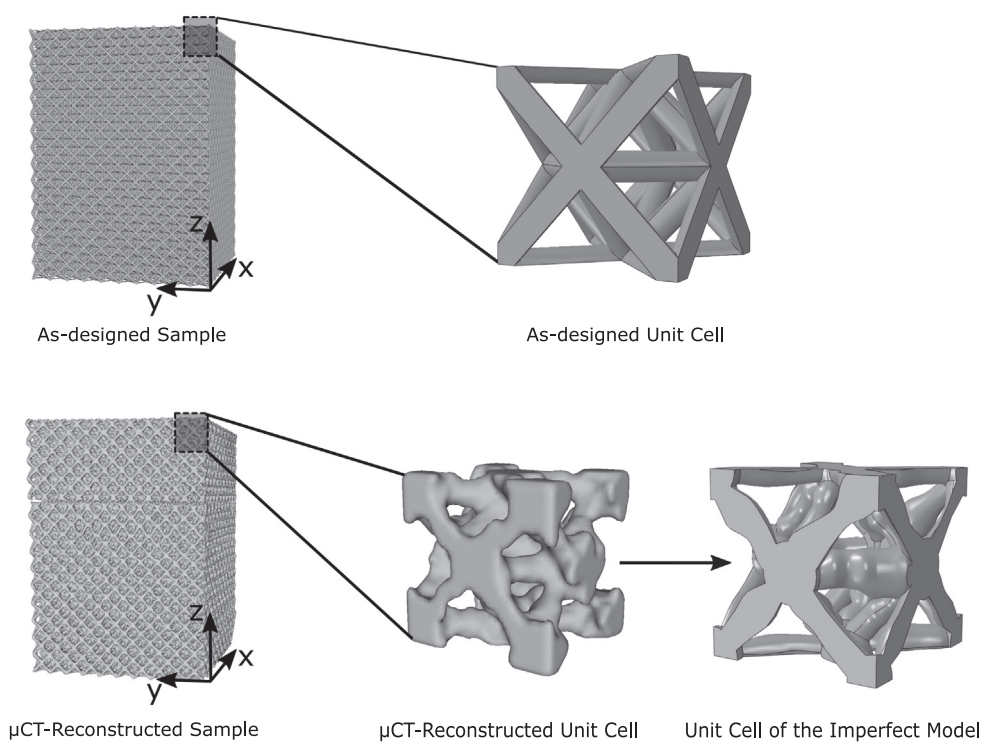

Fig. D.3. As-designed model, μCT-reconstructed unit cell, and representation of manufacturing defects on imperfect model for Octet #6.

function using a Kernel density estimation. This enables generation of numerical data (strut thickness and center deviation) that follow the imperfections distributions. Fig. D.2 presents the smoothed probability density distributions for the horizontal and diagonal struts of the Octet #6. These data are used via an in-house code as input in the computer aided design of each strut to create imperfect numerical models with porous architecture that is statistically similar to that of the as-manufactured one. Fig. D.3 presents the as-designed model with perfect-geometry of the unit cell, which serves as a reference for the computation of the mechanical properties. Unit cells of the μCT-reconstructed model and the imperfect-geometry model are also presented in Fig. D.1.

References

[1] S. Bose, S. Vahabzadeh, A. Bandyopadhyay, Bone tissue engineering using 3d printing, Mater. Today 16 (12) (2013) 496–504, https://doi.org/10.1016/j.mattod.2013.11.017. <Go to ISI>://WOS:000328640100018.

[2] J. Parthasarathy, 3d modeling, custom implants and its future perspectives in craniofacial surgery, Ann. Maxillofac. Surg. 4 (1) (2014) 9–18, https://doi.org/10.4103/2231-0746.133065. http://www.ncbi.nlm.nih.gov/pubmed/24987592.

[3] B. Levine, A new era in porous metals: Applications in orthopaedics, Adv. Eng. Mater. 10 (9) (2008) 788–792, https://doi.org/10.1002/adem.200800215. <Go to ISI>://WOS:000259934700004.

[4] J.D. Bobyn, R.M. Pilliar, H.U. Cameron, G.C. Weatherly, The optimum pore-size for the fixation of porous-surfaced metal implants by the ingrowth of bone, Clin. Orthopaed. Rel. Res. (150) (1980) 263–270. <Go to ISI>://WOS:A1980KD62000045.

[5] J.D. Bobyn, G.J. Stackpool, S.A. Hacking, M. Tanzer, J.J. Krygier, Characteristics of bone ingrowth and interface mechanics of a new porous tantalum biomaterial, J. Bone Jt. Surg. Br. 81B (5) (1999) 907–914, https://doi.org/10.1302/0301-620x.81b5.9283. <Go to ISI>://WOS:000082976700032.

[6] A.C. Jones, C.H. Arns, D.W. Hutmacher, B.K. Milthorpe, A.P. Sheppard, M.A. Knackstedt, The correlation of pore morphology, interconnectivity and physical properties of 3d ceramic scaffolds with bone ingrowth, Biomaterials 30 (7) (2009) 1440–1451, https://doi.org/10.1016/j.biomaterials.2008.10.056. <Go to ISI>://WOS:000263017800022.

[7] L.E. Murr, S.M. Gaytan, F. Medina, H. Lopez, E. Martinez, B.I. Machado, D.H. Hernandez, L. Martinez, M.I. Lopez, R.B. Wicker, J. Bracke, Next-generation biomedical implants using additive manufacturing of complex, cellular and functional mesh arrays, Philos. Trans. R. Soc. A 368 (1917) (2010) 1999–2032, https://doi.org/10.1098/rsta.2010.0010. <Go to WoS>://WOS:000286462200004.

[8] S. Arabnejad, R.B. Johnston, J.A. Pura, B. Singh, M. Tanzer, D. Pasini, High-strength porous biomaterials for bone replacement: a strategy to assess the interplay between cell morphology, mechanical properties, bone ingrowth and manufacturing constraints, Acta Biomater. 30 (2016) 345–356, https://doi.org/10.1016/j.actbio.2015.10.048. <Go to ISI>://WOS:000368563600031.

[9] J. Parthasarathy, B. Starly, S. Raman, A. Christensen, Mechanical evaluation of porous titanium (ti6al4v) structures with electron beam melting (ebm), J. Mech. Behav. Biomed. Mater. 3 (3) (2010) 249–259, https://doi.org/10.1016/j.jmbbm.2009.10.006. <Go to ISI>://WOS:000274716400003.

[10] S.A. Khanoki, D. Pasini, Multiscale design and multiobjective optimization of orthopedic hip implants with functionally graded cellular material, J. Biomech. Eng. Trans. ASME 134 (3) (2012) 10, https://doi.org/10.1115/1.4006115. <Go to ISI>://WOS:000302583200004..

[11] S.A. Khanoki, D. Pasini, The fatigue design of a bone preserving hip implant with functionally graded cellular material, J. Med. Devices Trans. ASME 7 (2) (2013) 2. <Go to ISI>://WOS:000326117600008.

[12] J.D. Bobyn, E.S. Mortimer, A.H. Glassman, C.A. Engh, J.E. Miller, C.E. Brooks, Producing and avoiding stress shielding - laboratory and clinical observations of noncemented total hip-arthroplasty, Clin. Orthopaed. Rel. Res. (274) (1992) 79–96. <Go to ISI>://WOS:A1992GY54900010.

[13] G. Ryan, A. Pandit, D.P. Apatsidis, Fabrication methods of porous metals for use in orthopaedic applications, Biomaterials 27 (13) (2006) 2651–2670, https://doi.org/10.1016/j.biomaterials.2005.12.002. <Go to ISI>://WOS:000235862600001.

[14] J.M. Sobral, S.G. Caridade, R.A. Sousa, J.F. Mano, R.L. Reis, Three-dimensional plotted scaffolds with controlled pore size gradients: effect of scaffold geometry on mechanical performance and cell seeding efficiency, Acta Biomater. 7 (3) (2011) 1009–1018, https://doi.org/10.1016/j.actbio.2010.11.003. http://www.ncbi.nlm.nih.gov/pubmed/21056125.

[15] A.K. Khoda, I.T. Ozbolat, B. Koc, Engineered tissue scaffolds with variational porous architecture, J. Biomech. Eng. 133 (1) (2011) 011001, https://doi.org/10.1115/1.4002933. http://www.ncbi.nlm.nih.gov/pubmed/21186891.

[16] E. Marin, S. Fusi, M. Pressacco, L. Paussa, L. Fearizzi, Characterization of cellular solids in ti6al4v for orthopaedic implant applications: trabecular titanium, J. Mech. Behav. Biomed. Mater. 3 (5) (2010) 373–381, https://doi.org/10.1016/j.jmbbm.2010.02.001. <Go to ISI>://WOS:000277947400002.

[17] S.J. Hollister, W.L. Murphy, Scaffold translation: barriers between concept and clinic, Tissue Eng. Part B 17 (6) (2011) 459–474, https://doi.org/10.1089/ten.teb.2011.0251. <Go to ISI>://WOS:000297326900010.

[18] S.L. Wu, X.M. Liu, K.W.K. Yeung, C.S. Liu, X.J. Yang, Biomimetic porous scaffolds for bone tissue engineering, Mater. Sci. Eng. R 80 (2014) 1–36, https://doi.org/10.1016/j.mser.2014.04.001. <Go to ISI>://WOS:000337931600001.

[19] S. Arabnejad, B. Johnston, M. Tanzer, D. Pasini, Fully porous 3d printed titanium femoral stem to reduce stress-shielding following total hip arthroplasty, J. Orthop. Res. (in press). doi:10.1002/jor.23445. https://www.ncbi.nlm.nih.gov/pubmed/27664796.

[20] A. Braem, A. Chaudhari, M. Vivan Cardoso, J. Schrooten, J. Duyck, J. Vleugels, Peri- and intra-implant bone response to microporous ti coatings with surface modification, Acta Biomater. 10 (2) (2014) 986–995, https://doi.org/10.1016/j.actbio.2013.10.017. http://www.ncbi.nlm.nih.gov/pubmed/24161385.

[21] Y. Kuboki, Q.M. Jin, H. Takita, Geometry of carriers controlling phenotypic expression in bmp-induced osteogenesis and chondrogenesis, J. Bone Jt. Surg. 83A (2001) S105–S115. <Go to ISI>://WOS:000168169500005.

[22] S.F. Yang, K.F. Leong, Z.H. Du, C.K. Chua, The design of scaffolds for use in tissue engineering. part 1. Traditional factors, Tissue Eng. 7 (6) (2001) 679–689, https://doi.org/10.1089/107632701753337645. <Go to ISI>://WOS:000172903100001.

[23] Z. Zhang, D. Jones, S. Yue, P.D. Lee, J.R. Jones, C.J. Sutcliffe, E. Jones, Hierarchical tailoring of strut architecture to control permeability of additive manufactured titanium implants, Mater. Sci. Eng. C 33 (7) (2013) 4055–4062, https://doi.org/10.1016/j.mSection 2013.05.050. http://www.ncbi.nlm.nih.gov/pubmed/23910314.

[24] S. Bernard, Q. Grimal, P. Laugier, Accurate measurement of cortical bone elasticity tensor with resonant ultrasound spectroscopy, J. Mech. Behav. Biomed. Mater. 18 (2013) 12–19, https://doi.org/10.1016/j.jmbbm.2012.09.017. http://www.ncbi.nlm.nih.gov/pubmed/23237876.

[25] C.Y. Lin, N. Kikuchi, S.J. Hollister, A novel method for biomaterial scaffold internal architecture design to match bone elastic properties with desired porosity, J. Biomech. 37 (5) (2004) 623–636, https://doi.org/10.1016/j.jbiomech.2003.09.029. http://www.ncbi.nlm.nih.gov/pubmed/15046991.

[26] L. Dong, V. Deshpande, H. Wadley, Mechanical response of ti-6al-4v octet-truss lattice structures, Int. J. Solids Struct. 60–61 (2015) 107–124, https://doi.org/10.1016/j.ijsolstr.2015.02.020. <Go to ISI>://WOS:000351962800011.

[27] V.S. Deshpande, M.F. Ashby, N.A. Fleck, Foam topology bending versus stretching dominated architectures, Acta Mater. 49 (6) (2001) 1035–1040, https://doi.org/10.1016/s1359-6454(00)00379-7. <Go to ISI>://WOS:000168027700010.

[28] V.S. Deshpande, N.A. Fleck, M.F. Ashby, Effective properties of the octet-truss lattice material, J. Mech. Phys. Solids 49 (8) (2001) 1747–1769, https://doi.org/10.1016/s0022-5096(01)00010-2. <Go to ISI>://WOS:000169805700006.

[29] O.L.A. Harrysson, O. CansiZoglu, D.J. Marcellin-Little, D.R. Cormier, H.A. West, Direct metal fabrication of titanium implants with tailored materials and mechanical properties using electron beam melting technology, Mater. Sci. Eng. C 28 (3) (2008) 366–373, https://doi.org/10.1016/j.mSection 2007.04.022. <Go to ISI>://WOS:000255451100009.

[30] P. Heinl, L. Muller, C. Korner, R.F. Singer, F.A. Muller, Cellular ti-6al-4v structures with interconnected macro porosity for bone implants fabricated by selective electron beam melting, Acta Biomater. 4 (5) (2008) 1536–1544, https://doi.org/10.1016/j.actbio.2008.03.013. <Go to ISI>://WOS:000259740400043.

[31] Mechanical testing of metals – Ductility testing – Compression test for porous and cellular metals, Standard, International Organization for Standardization, Geneva, CH (Dec. 2011).

[32] C.L. Lin, J.D. Miller, Network analysis of filter cake pore structure by high resolution x-ray microtomography, Chem. Eng. J. 77 (1–2) (2000) 79–86, https://doi.org/10.1016/s1385-8947(99)00149-7. <Go to ISI>://WOS:000085919400014.

[33] B. Vrancken, L. Thijs, J.P. Kruth, J. Van Humbeeck, Heat treatment of ti6al4v produced by selective laser melting: microstructure and mechanical properties, J. Alloys Compd. 541 (2012) 177–185, https://doi.org/10.1016/j.jallcom.2012.07.022. <Go to ISI>://WOS:000308868300032.

[34] RENISHAW, Ti6Al4V ELI-0406 powder for additive manufacturing (2016).

[35] Standard Test Methods for Tension Testing of Metallic Materials, Standard, ASTM International, West Conshohocken, PA (2016).

[36] R.G. Cowper, The shear coefficient in timoshenko's beam theory, J. Appl. Mech. 33 (1966) 335–340.

[37] S. Arabnejad, D. Pasini, Mechanical properties of lattice materials via asymptotic homogenization and comparison with alternative homogenization methods, Int. J. Mech. Sci. 77 (2013) 249–262, https://doi.org/10.1016/j.ijmecsci.2013.10.003. <Go to ISI>://WOS:000328710400025.

[38] T.M. Mower, M.J. Long, Mechanical behavior of additive manufactured, powder-bed laser-fused materials, Mater. Sci. Eng. A 651 (2016) 198–213, https://doi.org/10.1016/j.msea.2015.10.068. http://www.sciencedirect.com/science/article/pii/S092150931530530X.

[39] L. Liu, P. Kamm, F. Garca-Moreno, J. Banhart, D. Pasini, Elastic and failure response of imperfect three-dimensional metallic lattices: the role of geometric defects induced by selective laser melting, J. Mech. Phys. Solids 107 (2017) 160–184, https://doi.org/10.1016/j.jmps.2017.07.003. http://www.sciencedirect.com/science/article/pii/S0022509616307608.

[40] G.E. Ryan, A.S. Pandit, D.P. Apatsidis, Porous titanium scaffolds fabricated using a rapid prototyping and powder metallurgy technique, Biomaterials 29 (27)

(2008) 3625–3635, https://doi.org/10.1016/j.biomaterials.2008.05.032. http://www.ncbi.nlm.nih.gov/pubmed/18556060.
[41] J. Yang, H. Cai, J. Lv, K. Zhang, H. Leng, C. Sun, Z. Wang, Z. Liu, In vivo study of a self-stabilizing artificial vertebral body fabricated by electron beam melting, Spine (Phila Pa 1976) 39 (8) (2014) E486–E492, https://doi.org/10.1097/BRS.0000000000000211. http://www.ncbi.nlm.nih.gov/pubmed/24430723.
[42] L.J. Gibson, M.F. Ashby, Cellular Solids: Structure and Properties, Cambridge, 1999.
[43] A. Vigliotti, D. Pasini, Linear multiscale analysis and finite element validation of stretching and bending dominated lattice materials, Mech. Mater. 46 (2012) 57–68, https://doi.org/10.1016/j.mechmat.2011.11.009. <Go to ISI>://WOS:000301018800006.
[44] D.K. Pattanayak, A. Fukuda, T. Matsushita, M. Takemoto, S. Fujibayashi, K. Sasaki, N. Nishida, T. Nakamura, T. Kokubo, Bioactive ti metal analogous to human cancellous bone: Fabrication by selective laser melting and chemical treatments, Acta Biomater. 7 (3) (2011) 1398–1406, https://doi.org/10.1016/j.actbio.2010.09.034. http://www.ncbi.nlm.nih.gov/pubmed/20883832.
[45] C.Z. Yan, L. Hao, A. Hussein, D. Raymont, Evaluations of cellular lattice structures manufactured using selective laser melting, Int. J. Mach. Tools Manuf. 62 (2012) 32–38, https://doi.org/10.1016/j.ijmachtools.2012.06.002. <Go to ISI>://WOS:000308451400004.
[46] M.R.K. Ravari, M. Kadkhodaei, M. Badrossamay, R. Rezaei, Numerical investigation on mechanical properties of cellular lattice structures fabricated by fused deposition modeling, Int. J. Mech. Sci. 88 (2014) 154–161, https://doi.org/10.1016/j.ijmecsci.2014.08.009. <Go to ISI>://WOS:000344428000017.
[47] G. Campoli, M.S. Borleffs, S.A. Yavari, R. Wauthle, H. Weinans, A.A. Zadpoor, Mechanical properties of open-cell metallic biomaterials manufactured using additive manufacturing, Mater. Des. 49 (2013) 957–965, https://doi.org/10.1016/j.matdes.2013.01.071. <Go to ISI>://WOS:000318547000116.
[48] M. Fini, G. Giavaresi, P. Torricelli, V. Borsari, R. Giardino, A. Nicolini, A. Carpi, Osteoporosis and biomaterial osteointegration, Biomed. Pharmacother. 58 (9) (2004) 487–493, https://doi.org/10.1016/j.biopha.2004.08.016. <Go to ISI>://WOS:000225352000001.
[49] S. Van Bael, G. Kerckhofs, M. Moesen, G. Pyka, J. Schrooten, J.P. Kruth, Micro-ct-based improvement of geometrical and mechanical controllability of selective laser melted ti6al4v porous structures, Mater. Sci. Eng. A 528 (24) (2011) 7423–7431, https://doi.org/10.1016/j.msea.2011.06.045. <Go to ISI>://WOS:000294091900042.
[50] C.A. Engh, J.D. Bobyn, A.H. Glassman, Porous-coated hip-replacement – the factors governing bone ingrowth stress shielding and clinical-results, J. Bone Jt. Surg. 69 (1) (1987) 45–55. <Go to ISI>://WOS:A1987F756800011.
[51] A.J.W. Johnson, B.A. Herschler, A review of the mechanical behavior of cap and cap/polymer composites for applications in bone replacement and repair, Acta Biomater. 7 (1) (2011) 16–30, https://doi.org/10.1016/j.actbio.2010.07.012. <Go to ISI>://WOS:000284795300002.
[52] Z.S. Bagheri, D. Melancon, L. Liu, R.B. Johnston, D. Pasini, Compensation strategy to reduce geometry and mechanics mismatches in porous biomaterials built with selective laser melting, J. Mech. Behav. Biomed. Mater. 70 (2017) 17–27, https://doi.org/10.1016/j.jmbbm.2016.04.041. mechanics of additively manufactured biomaterials and implants. http://www.sciencedirect.com/science/article/pii/S175161611630114X.
[53] C. Qiu, S. Yue, N.J. Adkins, M. Ward, H. Hassanin, P.D. Lee, P.J. Withers, M.M. Attallah, Influence of processing conditions on strut structure and compressive properties of cellular lattice structures fabricated by selective laser melting, Mater. Sci. Eng. A 628 (2015) 188–197, https://doi.org/10.1016/j.msea.2015.01.031. http://www.sciencedirect.com/science/article/pii/S0921509315000453.
[54] A. Shiraziadl, M. Dammak, G. Paiement, Experimental-determination of friction characteristics at the trabecular bone porous-coated metal interface in cementless implants, J. Biomed. Mater. Res. 27 (2) (1993) 167–175, https://doi.org/10.1002/jbm.820270205. <Go to ISI>://WOS:A1993KG41000004.
[55] Y. Zhang, P.B. Ahn, D.C. Fitzpatrick, A.D. Heiner, R.A. Poggie, T.D. Brown, Interfacial frictional behavior: cancellous bone, cortical bone, and a novel porous tantalum biomaterial, J. Musculoskel. Res. 3 (4) (1999) 245–251, https://doi.org/10.1142/S0218957799000269. http://www.worldscientific.com/doi/abs/10.1142/S0218957799000269.
[56] B.R. Levine, S. Sporer, R.A. Poggie, C.J. Della Valle, J.J. Jacobs, Experimental and clinical performance of porous tantalum in orthopedic surgery, Biomaterials 27 (27) (2006) 4671–4681, https://doi.org/10.1016/j.biomaterials.2006.04.041. <Go to ISI>://WOS:000239291300001.
[57] H.A. Ching, D. Choudhury, M.J. Nine, N.A. Abu, Osman, Effects of surface coating on reducing friction and wear of orthopaedic implants, Sci. Technol. Adv. Mater. 15 (1) (2014) 21, https://doi.org/10.1088/1468-6996/15/1/014402. <Go to ISI>://WOS:000332466700013.
[58] J.D. Bobyn, G.J. Stackpool, S.A. Hacking, M. Tanzer, J.J. Krygier, Characteristics of bone ingrowth and interface mechanics of a new porous tantalum biomaterial, J. Bone Jt. Surg. Br. 81 (5) (1999) 907–914.
[59] G. Lewis, Properties of open-cell porous metals and alloys for orthopaedic applications, J. Mater. Sci. 24 (10) (2013) 2293–2325, https://doi.org/10.1007/s10856-013-4998-y.
[60] DePuy Synthes, Product Rationale GRIPTION (2014).
[61] Stryker, Tritanium PL Posterior Lumbar Cage Technical Summary (2017).
[62] M.R. Dias, J.M. Guedes, C.L. Flanagan, S.J. Hollister, P.R. Fernandes, Optimization of scaffold design for bone tissue engineering: a computational and experimental study, Med. Eng. Phys. 36 (4) 448–457, iSI Document Delivery No.: AF8OZ ISSN = 1350–4533, doi:10.1016/j.medengphy.2014.02.010, URL: <Go to ISI>://WOS:000334976800005, year = 2014, type = Journal Article.
[63] X. Cheng, S. Li, L. Murr, Z. Zhang, Y. Hao, R. Yang, F. Medina, R. Wicker, Compression deformation behavior of ti6al4v alloy with cellular structures fabricated by electron beam melting, J. Mech. Behav. Biomed. Mater. 16 (2012) 153–162, https://doi.org/10.1016/j.jmbbm.2012.10.005. http://www.sciencedirect.com/science/article/pii/S1751616112002639.
[64] F. Bobbert, K. Lietaert, A. Eftekhari, B. Pouran, S. Ahmadi, H. Weinans, A. Zadpoor, Additively manufactured metallic porous biomaterials based on minimal surfaces: a unique combination of topological, mechanical, and mass transport properties, Acta Biomater. 53 (2017) 572–584, https://doi.org/10.1016/j.actbio.2017.02.024. http://www.sciencedirect.com/science/article/pii/S1742706117301290.
[65] M. Atsumi, S.H. Park, H.L. Wang, Methods used to assess implant stability: current status, Int. J. Oral Maxillofac. Implants 22 (5) (2007) 743–754.
[66] S.A. Yavari, S.M. Ahmadi, R. Wauthle, B. Pouran, J. Schrooten, H. Weinans, A.A. Zadpoor, Relationship between unit cell type and porosity and the fatigue behavior of selective laser melted meta-biomaterials, J. Mech. Behav. Biomed. Mater. 43 (2015) 91–100, https://doi.org/10.1016/j.jmbbm.2014.12.015. <Go to ISI>://WOS:000349512300009.
[67] J.M. Guedes, N. Kikuchi, Preprocessing and postprocessing for materials based on the homogenization method with adaptive finite-element methods, Comput. Methods Appl. Mech. Eng. 83 (2) (1990) 143–198, https://doi.org/10.1016/0045-7825(90)90148-f. <Go to ISI>://WOS:A1990EG31800004.
[68] S.J. Hollister, N. Kikuchi, A comparison of homogenization and standard mechanics analyses for periodic porous composites, Comput. Mech. 10 (2) (1992) 73–95, https://doi.org/10.1007/BF00369853.
[69] B. Hassani, A direct method to derive the boundary conditions of the homogenization equation for symmetric cells, Communications in Numerical Methods in Engineering 12 (3). doi:10.1002/(SICI)1099-0887(199603)12:3185::AID-CNM9703.0.CO;2-2. doi: 10.1002/(SICI)1099-0887(199603)12:3185::AID-CNM9703.0.CO;2-2.